STRUCTURAL ASYMMETRY OF FLAVIVIRUSES

by

Matthew D. Therkelsen

A Dissertation

Submitted to the Faculty of Purdue University

In Partial Fulfillment of the Requirements for the degree of

Doctor of Philosophy

Department of Biological Sciences

West Lafayette, Indiana

May 2019

THE PURDUE UNIVERSITY GRADUATE SCHOOL
STATEMENT OF COMMITTEE APPROVAL

Dr. Richard J. Kuhn, Chair
Department of Biological Sciences
Dr. Michael G. Rossmann
Department of Biological Sciences
Dr. Garth J. Simpson
Department of Chemistry
Dr. Nicholas Noinaj
Department of Biological Sciences

Approved by:

Dr. Janice Evans
Head of the Graduate Program

To Talia

ACKNOWLEDGMENTS

I would like to thank Richard Kuhn for welcoming me into his lab and providing a great lab environment for me to incubate and grow in. His ability to synthesize my scattered ideas into practical hypotheses and techniques was awe-inspiring, and I appreciate that he always supported me in pursuing the twists and turns in my research. He was also a strong advocate for me to share my research with others, and I'm grateful for the opportunities I had to present at ASV and FASEB conferences. His east coast sarcasm made the lab feel like home.

I would like to thank Michael Rossmann for pushing me to tackle the seemingly impossible and for instilling a sense of wonder into my research. When I did not understand how a subtomogram averaging program worked, he told me, "scientists should write their own programs." I followed his advice, and even though my MATLAB program is still a work-in-progress, the coding process gave me a better understanding of how to optimize other programs.

Additionally, I would like to thank my committee members Garth Simpson, Ji-Xin Cheng, and Nick Noinaj for their questions and support. They helped teach me to communicate the story along with the technical details during a presentation, and reminded me to be thorough and rigorous in my research.

I would like to acknowledge the administrators, research scientists, collaborators, colleagues, and staff members who made sure that my research and training went smoothly. This includes Valorie Bowman, Sheryl Kelly, Steve Wilson, Becky Harding, Russell Logsdon, Vicki Hedricks, Uma Aryal, and Tiago Paschoal Sobreira. I'd like to especially thank Thomas Klose for answering my incessant questions and providing feedback on the manuscript and my dissertation. I would like to thank Frank Vago for helping me to collect data late at night and for teaching me tips and tricks on data processing. I would like to thank Wen Jiang and Cynthia Stauffacher for

discussing results and brainstorming ideas with me. A huge thanks to Anita Robinson for keeping me on track and helping me sort out administrative issues.

I would like to thank my labmates and colleagues Devika Sirohi, Conrrad Nicholls, Shishir Poudyal, Jeff Grabowski, Adriano Mendes, Thu Cao, Mike Dibiasio-White, Ampa Suksatu, Crysta Colangelo, Jinsam Chang, Carlos Brito, Tom Edwards, Diego Coelho, Amarilis Giaretta de Moraes, Matt Lerdahl, Tara Temkar, Vedita Singh, and Joyce Jose who questioned my experiments and results and offered great suggestions about how to proceed. Thank you to Andy Miller; on top of being an entertaining BSL2 companion, he always made sure I had the necessary reagents and kept the lab running smoothly. Thu Cao, Shishir Poudyal, Mike Dibiaso-White, and Adriano Mendes get a second mention for being part of the Lavazza crew, as coffee was an essential component of my research. I'd like to thank my undergraduates Ena Tully and Hunter Wieczorek, for their hard work and for the fun conversations we had in the office.

I would like to thank Carol Post for helping to organize the Hock Socials and for our great discussions on flaviviruses. I'd like to thank the social committee members and my friends, Brandon Anson, Lizzy Garland-Kuntz, Joz Clasman, Frank Vago, Adriano Mendes, Corey Moore, Veronica Heintz, Lenna Peterson, and Carlos Brito. I'd like to thank Jake Werth for all the great times playing music around Lafayette, and Adam Hamdani for the beat-making sessions.

The members of the Rossmann lab were a great source of knowledge and I am thankful for their advice and help. In particular Yue Liu offered many suggestions on data processing, and Charles-Adrien Arnaud gave me helpful feedback on my work. I would also like to thank Qianglin Fang, Andrei Fokine, Madhu Sevvana, Geeta Buda, Baldeep Khare, S. Saif Hasan for advice and help with data analysis.

I would like to thank my parents and siblings for their unwavering support and enthusiasm about my progress. I appreciate their willingness to listen to even the most minor of details about my research. Additionally, I would like to thank my grandparents and my extended family for their love and support, and for visiting me out in Indiana. I would like to thank V. and Bialy, for their entertaining animal silliness. I would lastly like to thank Talia Steiman, to whom this work is dedicated, for encouraging me to pursue graduate school, and who is my sharpest, loving critic.

TABLE OF CONTENTS

LIST OF TABLES

LIST OF FIGURES

LIST OF ABBREVIATIONS

ABC	ammonium bicarbonate
ACN	acetonitrile
BCA	bicinchoninic acid
BSA	bovine serum albumin
C	capsid
CP3	cryoplunge 3
CPE	cytopathic effect
Cryo-EM	cryo-electron microscopy
CSTA	cystatin-A
DENV	dengue virus
DENV-1	dengue virus, serotype 1
DENV-2	dengue virus, serotype 2
DHF	dengue hemorrhagic fever
DI	domain I
DII	domain II
DIII	domain III
DMEM	Dulbecco's modified Eagle medium
DSS	dengue shock syndrome
DTT	dithiothreitol
E	envelope
ECE1	endothelin converting enzyme 1
EDTA	ethylenediaminetetraacetic acid
EM	electron microscopy
ER	endoplasmic reticulum
ESCRT	endosomal sorting complexes required for transport
EVs	extracellular vesicles
Fab	fragment, antigen-binding
FBS	fetal bovine serum
FGB	fibrinogen beta chain
FLNB	filamin B, beta
FSC	Fourier shell correlation
GO	gene ontology
HBV	hepatitis B virus
HCD	higher-energy C-trap dissociation
HCV	hepatitis C virus
HEK 293T	human embryonic kidney 293T cells
HEPES	4-(2-hydroxyethyl)-1-piperazineethanesulfonic acid
HIV-1	human immunodeficiency virus 1
Huh-7	human hepatocellular carcinoma cells
JEV	Japanese encephalitis virus
kDa	kilodalton
KUNV	Kunjin virus
LC-MS/MS	liquid chromatography-tandem mass spectrometry

LFQ	label free quantification
M	membrane
mAb	monoclonal antibody
MEM	minimal essential media
MOI	multiplicity of infection
NEAA	non-essential amino acids
NMR	nuclear magnetic resonance
NS	nonstructural
NS1	nonstructural protein 1
PBS	phosphate-buffered saline
PBS-T	phosphate-buffered saline-tween
PEG	polyethylene glycol
pr	pre
prM	premembrane
RNA	ribonucleic acid
RPM	revolutions per minute
SDS-PAGE	sodium dodecyl sulfate-polyacrylamide gel electrophoresis
SGD	stochastic gradient descent
sp	species
SVPs	subviral particles
TGN	trans-Golgi network
WNV	West Nile virus
YFV	yellow fever virus
ZIKV	Zika virus

ABSTRACT

Author: Therkelsen, Matthew, D. PhD
Institution: Purdue University
Degree Received: May 2019
Title: Structural Asymmetry of Flaviviruses
Committee Chair: Richard J. Kuhn

Flaviviruses are enveloped, positive-strand RNA viruses that are spread by mosquitoes and ticks and can cause serious disease in humans. Flavivirus virions undergo extensive structural changes during their life cycle, including during maturation and fusion. Flaviviruses are initially assembled at the endoplasmic reticulum in a non-infectious, immature state, and then traffic to the trans-Golgi network, where a pH drop triggers a structural rearrangement of glycoproteins prM and E on the virus surface from 60 trimers to 90 dimers. A host protease, furin, then cleaves prM which makes the transition irreversible. Upon exiting the host cell, pr disassociates from the virus and the infectious, mature virus is able to enter a new cell.

In Chapter 1, an overview of flaviviruses is presented, including a brief history of their discovery and interaction with humans, followed by what is known about their life cycle and the maturation process. The structure of a mature flavivirus is then described, including the symmetrical arrangement of glycoproteins on the virion surface, the lipid membrane, and the nucleocapsid core, followed by an introduction of the structural proteins that assemble into the virion. The structure of the immature flavivirus is then described. The chapter concludes with a description of the dynamics and heterogeneity observed for flaviviruses.

The conformational rearrangements that occur during flavivirus maturation remain unclear. The structures of immature and mature flaviviruses determined with cryo-electron microscopy (cryo-EM) demonstrated that flaviviruses are icosahedral particles with 180 copies of

glycoproteins on their surface. Icosahedral viruses typically have a quasi-equivalent arrangement of glycoproteins, but flaviviruses lack quasi-equivalence and instead the three subunits within an asymmetric unit occupy different chemical environments. Although the subunits are the same proteins, the unique environment of each subunit can be exploited for tracking subunits during conformational rearrangements. For example, the unique labeling of a subunit can be used to identify it in the immature and mature virion.

In Chapter 2, the maturation process was studied by developing tools to differentially label protein subunits and trap potential intermediates of maturation. The tools included heavy-atom compounds and antibody Fabs, which were used to probe Kunjin virus (KUNV), an Australian subtype of West Nile virus (WNV). One heavy-atom compound, potassium tetranitroplatinate(II), was found to derivatize immature KUNV, likely at sites on both E and prM. Higher-resolution studies will be required to determine if the compound differentially labeled the three subunits. The other tool developed was the E16 Fab. E16 Fab, originally isolated from a mouse immunized with WNV E and found to bind to two out of three subunits on mature WNV, was used to differentially label subunits in immature KUNV. Based on poor epitope accessibility on immature KUNV, E16 Fab was hypothesized to trap an intermediate state of maturation. In the cryo-EM reconstruction of E16 Fab bound to immature KUNV it was found that the virion had localized distorted density and apparent non-uniform binding of the E16 Fab. Based on this result it was proposed that flaviviruses had imperfect icosahedral symmetry.

The structural asymmetry of immature and mature flaviviruses was investigated in Chapter 3. Icosahedral symmetry has always been imposed during cryo-EM reconstructions of flaviviruses, as it led to stable convergence of orientations. When reconstructions of immature KUNV and ZIKV were performed without imposing symmetry, the reconstructions showed that the

flaviviruses had an eccentric nucleocapsid core, which was positioned closer to the membrane at one pole. At the opposite pole, the glycoprotein and inner leaflet densities were weak and distorted. Furthermore, there were protrusions from the core that contacted the transmembrane helices of the glycoproteins. In the asymmetric reconstruction of mature KUNV, the core was positioned concentric with the glycoprotein shell, in contrast to the immature virion, indicating that maturation alters the interactions between the core and the glycoproteins. The asymmetric reconstructions suggested that there is variable contact between the core and glycoproteins during assembly, which may be due to membrane curvature restrictions in the budding process.

In Chapter 4, extracellular vesicles (EVs) that were released during dengue virus (DENV) infection were characterized by mass spectrometry. EVs may play a significant role in flavivirus infection, as they have been shown to transport both viral proteins and infectious RNA. EVs likely represent alternative modes of virus transmission and aid in immune evasion. However, previous studies on EVs are controversial because EVs are potential contaminated during assays by co-purifying virions and other particulates. The identification of EV biomarkers would greatly reduce contamination because biomarkers would enable isolation of pure EVs by affinity purification. Therefore, a strategy was developed to isolate EVs and profile them with proteomics. The four proteins cystatin-A, filamin B, fibrinogen beta chain, and endothelin converting enzyme 1 were found to be statistically enriched in the DENV sample and represent potential EV biomarkers.

CHAPTER 1. FLAVIVIRUSES

1.1 Introduction

Flaviviruses are enveloped, positive-strand RNA viruses that are transmitted by mosquitoes and ticks. These viruses cause serious disease in humans and represent a global public health challenge. Yellow fever virus (YFV) was the first reported flavivirus, and gave the *Flaviviridae* family its name: from the Latin *flavus,* "yellow". Other flaviviruses include West Nile virus (WNV), Zika virus (ZIKV), and dengue virus (DENV). A brief history of these viruses will be described.

WNV is transmitted by *Culex* sp mosquitoes and can cause encephalitis and meningitis. It was first introduced into the United States in the New York City area in 1999, where it led to 59 hospitalizations and seven deaths (1). The epidemic then spread across the east coast of the US between 1999 and 2002. Birds are the natural reservoir of WNV, and the virus was particularly virulent for birds in the family *Corvidae* such as crows and jays. Therefore a dead-bird-based surveillance program was used to track the spread of the virus (1). The WNV sp includes Kunjin virus (KUNV), an Australian subtype of WNV that in rare occasions can cause encephalitis (2). Due to its low virulence, KUNV has been used as a model system to study WNV.

ZIKV was first isolated in 1947 from a sentinel rhesus macaque kept in a cage on a platform in the Zika Forest in Uganda (3). The virus is transmitted by *A. aegypti* mosquitoes, and was not well studied until outbreaks began in 2007 in Yap Island in Micronesia (4). ZIKV was declared a public health emergency by the World Health Organization in 2016, and it was determined to cause microcephaly in developing fetuses (3).

A. aegypti mosquitoes also carry DENV, a virus which is localized in tropical and subtropical regions. DENV infection elicits muscle and joint pain referred to as break-bone fever.

There are four serotypes of DENV, and successive infections by different serotypes can lead to DENV hemorrhagic fever (DHF) and DENV shock syndrome (DSS) (5). The first DHF epidemic was recorded in the Philippines between 1953 and 1954 (6). There are an estimated 390 million cases of DENV each year, imposing a formidable public health burden on society (7).

1.2 Life Cycle

Flaviviruses enter a host cell by receptor-mediated endocytosis. Receptors for flaviviruses have not been identified, indicating that multiple receptors may be used. Once internalized inside the cell, the endosomal pH drops, triggering a conformational change of the viral glycoproteins from 90 dimers to 60 trimers, and insertion of fusion peptides into the endosomal membrane (8, 9). Fusion then occurs and the viral genome is released into the cell. As the ~11 kb viral genome is a positive-strand RNA, it can be immediately translated by ribosomes at the endoplasmic reticulum (ER). The genome contains one open reading frame that is translated as a polyprotein and cleaved by host and viral proteases into ten proteins, including the structural proteins envelope (E), premembrane (prM), and capsid (C), and the nonstructural (NS) proteins NS1, NS2A, NS2B, NS3, NS4A, NS4B, and NS5 (10). There are multiple signal sequences that direct the topology of the viral proteins as they are threaded through the ER (Figure 1.1). Once cleaved, the structural proteins will assemble into new viruses, while the nonstructural proteins will function in genome synthesis, assembly, and innate immune antagonism.

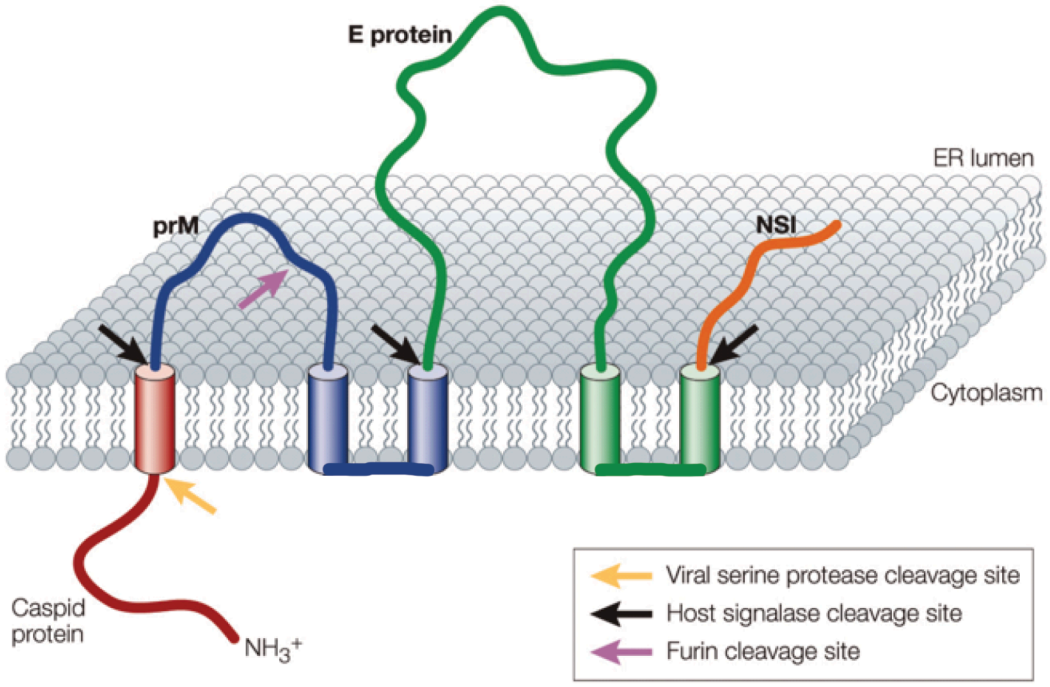

Figure 1.1 Translation of the flavivirus structural proteins at the ER

The flavivirus genome is translated as a polyprotein that initiates at the N-terminus with C, prM, and E. These proteins are threaded through the ER and contain signal sequences that are cleaved by both host signalase proteins and the viral protease. The turns in the transmembrane helices of prM and E do not extend into the cytoplasm and therefore do not directly interact with C. Adapted with permission from (11).

The ER is a major site of activity for flaviviruses, as both replication of genomes and assembly of new virions occur there. After an RNA genome is synthesized, C and RNA form a nucleocapsid core and interact with E and prM, which are arranged on the ER membrane, likely in trimeric arrays. The virion forms as the glycoprotein-decorated membrane envelopes the nucleocapsid core, budding into the ER and undergoing scission to complete assembly. This immature virus contains 60 copies of prM-E trimeric spikes arranged with icosahedral symmetry (12). The immature virion then traffics along the secretory pathway. When the virus enters the trans-Golgi network (TGN), it encounters low pH which causes a structural rearrangement on the

surface of the virus: the glycoproteins rearrange from 60 trimers to 90 dimers (Figure 1.2) (13). After this transition occurs, host furin cleaves prM into pr and M, irreversibly locking the virus into its mature state (13). pr stays attached to the virus until the virus exits the cell, at which point pr disassociates into the extracellular space (14). The mature virion then infects a new cell.

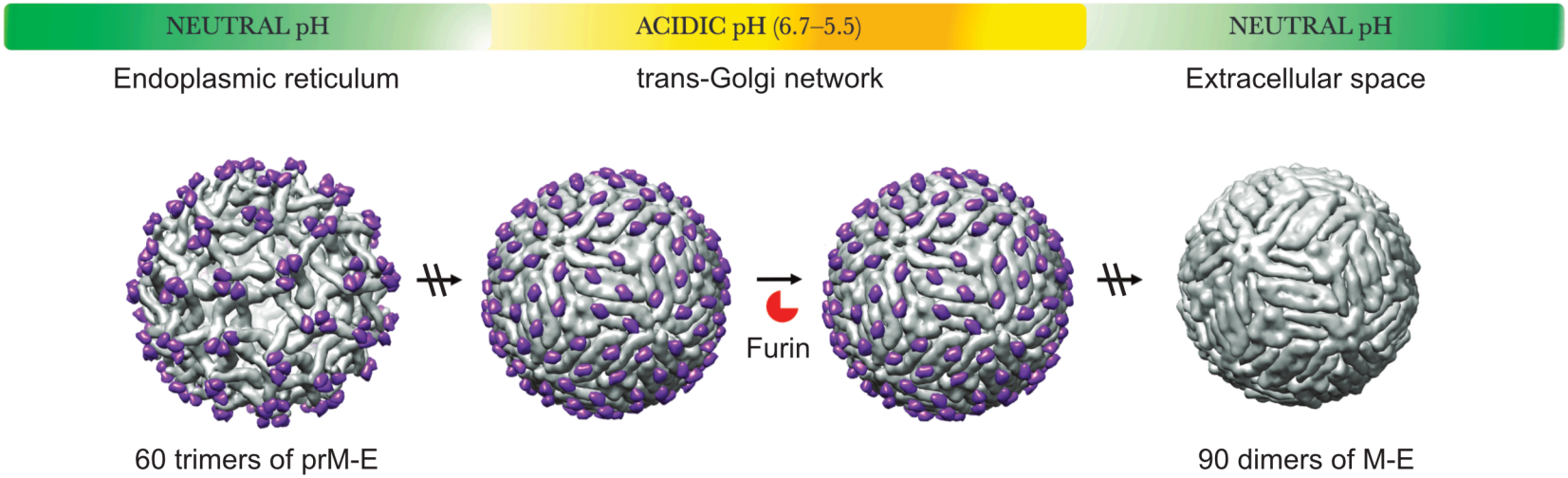

Figure 1.2 Maturation pathway of flaviviruses

Flavivirus maturation is required to produce infectious particles. The conformational rearrangement causes 60 trimers of prM-E to form 90 dimers, changing the virus morphology from "spiky" to "smooth". Low pH in the trans-Golgi network (TGN) triggers the rearrangement, which is then locked into place with furin cleavage of prM. Once the virus is released into the extracellular space, pr disassociates from the virus. Adapted with permission from (15).

1.3 Flavivirus Structure

The mature flavivirus is roughly spherical and ~50 nm in diameter. On the surface of the virus is an icosahedral arrangement of 180 copies of M and E glycoproteins that lie flat, giving the virion a smooth appearance (Figure 1.3) (16). The glycoproteins are dimers and arranged in closely packed “rafts”. There are three sets of dimers in a raft that run roughly parallel, and 30 rafts constitute the virus surface and are arranged in a herringbone pattern. Within a raft, one set of dimers is positioned on an icosahedral twofold axis, with the neighboring dimer sets on quasi-twofold axes. The icosahedral arrangement of the glycoproteins includes 12 vertices with fivefold rotational symmetry, 20 triangular faces with threefold rotational symmetry, and 30 edges with twofold rotational symmetry (17).

The asymmetric unit contains three subunits of M-E and 60 identical asymmetric units of these subunits constitute the virus surface. Casper & Klug quasi-equivalence theory for icosahedral viruses predicts that identical protein subunits will have slightly different environments due to their packing arrangement (18–20). However, for flaviviruses it was found that subunits have non-equivalent contacts with adjacent subunits and therefore each subunit resides in a completely different chemical environment (16). The non-equivalence of flaviviruses influences antibody binding and neutralization, and can result in variable occupancy of epitopes (21).

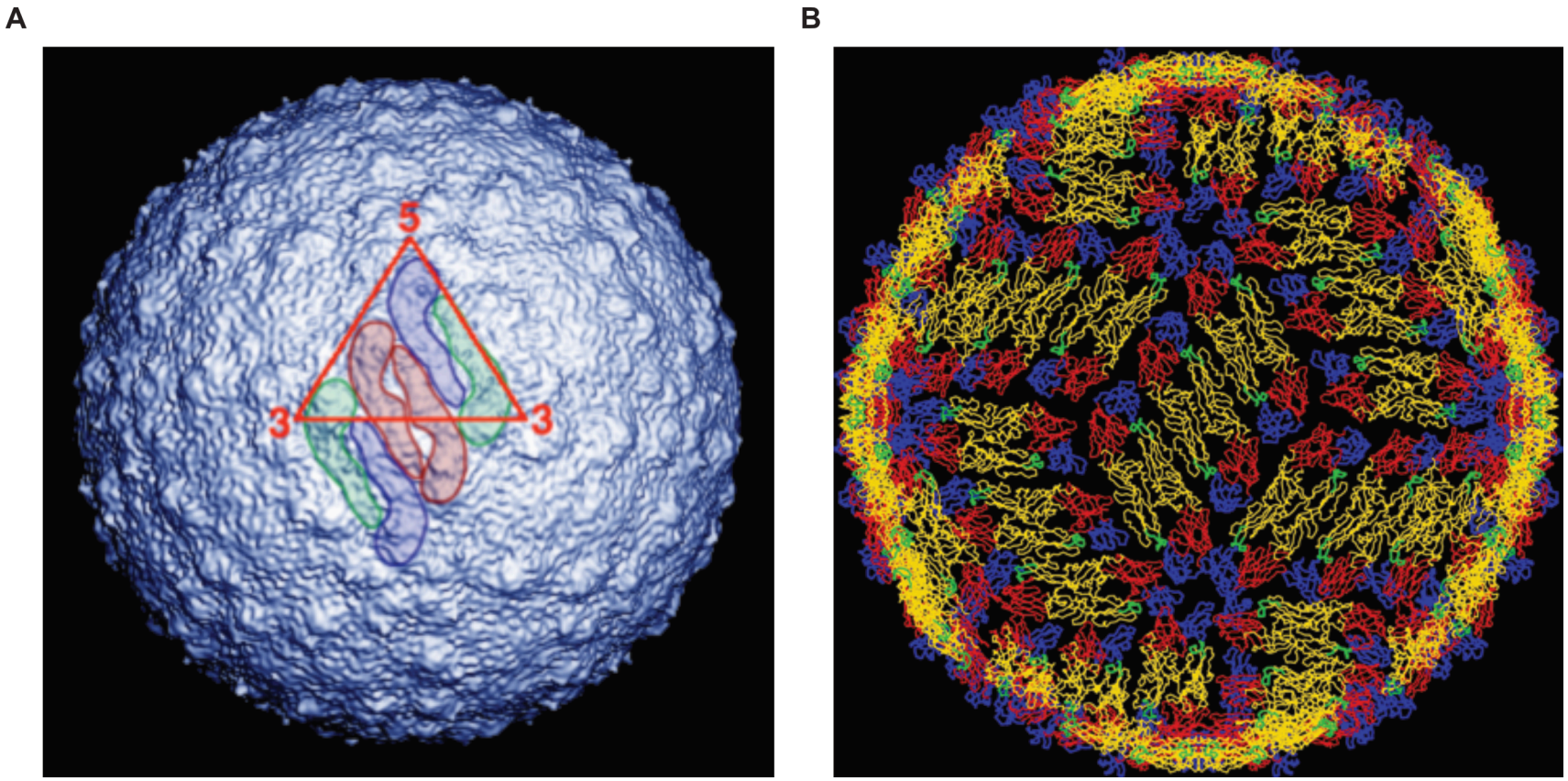

Figure 1.3 Structure of a mature flavivirus

Mature flaviviruses have a smooth appearance with subunits arranged in a herringbone pattern. (**A**) Surface view of a mature DENV cryo-EM reconstruction showing three subunits within an asymmetric unit. The asymmetric unit is indicated by a red triangle. The non-equivalent subunits are colored green, blue, and red. (**B**) E fitted into the cryo-EM reconstruction showing the packing arrangement of glycoproteins. The individual domains of E are colored red, yellow, and blue for DI, DII, and DIII, respectively. The fusion peptide located at the tip of DII is colored green. Adapted with permission from (16).

The structures of mature DENV, ZIKV, WNV, and Japanese encephalitis virus (JEV) appear essentially the same, despite these viruses having distinct tropisms and disease outcomes (16, 22–24). One difference in the virions that could help explain their unique pathogenesis is E glycosylation. When comparing ZIKV to DENV, it was noted that the largest difference in the structures was at the glycosylation site at N154 (22). Glycosylation status differs among flaviviruses, as DENV is glycosylated at N153 and N67, while WNV and ZIKV are glycosylated at N154. The glycosylation site and surrounding region in ZIKV were hypothesized to enable ZIKV to cross the placental barrier and infect fetal brains (15). Unique structural features in addition to the glycosylation site may be present in flaviviruses, but have possibly been hidden by icosahedral symmetry constraints that were imposed when calculating cryo-EM reconstructions.

The glycoprotein shell of a flavivirus virion is composed of two glycoproteins M and E (Figure 1.4). Both are membrane proteins with two transmembrane helices that act as double membrane anchors. The ectodomain of E consists of a stem region and three domains I, II, and III (DI, DII, and DIII). DI is an eight stranded β-barrel, DII has a long, finger-like domain, and DIII has an immunoglobin-like domain (25). DI, DII, and DIII function in viral conformational rearrangements, fusion, and receptor engagement, respectively.

M is initially translated as prM and sits on top of the fusion peptide of E in the immature virus preventing premature fusion of the virus with the producer cell. After furin cleavage of prM, the remaining ectodomain of M is a short sequence (38 amino acids in DENV) which has a weakly amphipathic alpha-helix and been hypothesized to act as a drawstring to facilitate the conformational rearrangements of E protein (26).

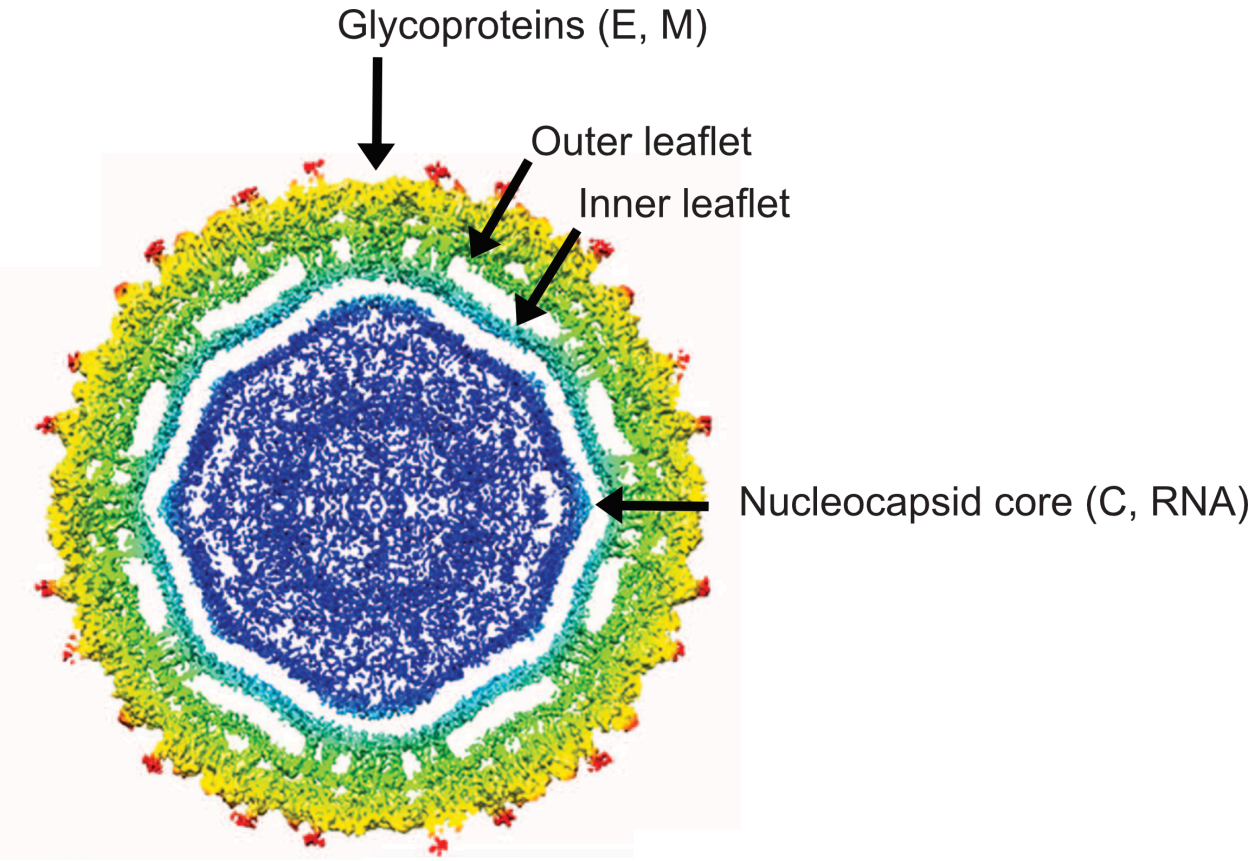

Figure 1.4 Composition of a flavivirus

Cross-section of a mature ZIKV cryo-EM reconstruction, colored radially. The nucleocapsid core (dark blue) is located inside the virion and contains the single-stranded RNA genome and C. Enclosing the core is a lipid bilayer, composed of an inner (cyan) and outer leaflet (green). The transmembrane helices of E and M traverse the lipid bilayer. On the exterior of the virus, the glycoprotein shell contains E and M (yellow, with red-colored glycans). Adapted with permission from (22).

The lipid bilayer in the virion is approximately 45 Å thick, consistent with lipid bilayers found within a cell (16). In the mature virus the bilayer is polygonal shaped, from the transmembrane helices which constrict localized regions of the membrane. In general, the arrangement of the glycoproteins controls membrane curvature (27). 12 transmembrane helices traverse the membrane within an asymmetric unit, and four helices are associated with each M-E heterodimer (28). The position of the transmembrane helices is the same for dimers located at the

icosahedral twofold and the quasi-twofold. The transmembrane helices do not extend beyond the bilayer to make contact with C (28).

Underneath the virion membrane is the nucleocapsid core composed of the single-stranded RNA genome and C. No discernable organization of the core has been identified in cryo-EM reconstructions (29). Furthermore, a gap of ~15 Å separates the inner leaflet and the nucleocapsid core, making it unclear how the core could interact with the membrane (28). C is a highly basic, alpha-helical protein that was shown to be a dimer in solution and was hypothesized to interact with RNA on one side and membrane on the other side (30).

1.4 Immature Flavivirus Structure

The immature virus is ~60 nm in diameter and is composed of 60 trimeric projections of prM-E, giving the virus a "spiky" appearance (Figure 1.5) (12). The protein subunits are arranged with icosahedral symmetry, but the overall structure is distinct from the herringbone pattern seen in the mature virus. Instead, the subunits are arranged as an interwoven lattice, with DIII of one E contacting the base of E DII in an adjacent spike (31). As the subunits are more loosely packed than in the mature virus, there is exposed lipid membrane on the virus surface.

The asymmetric unit of an immature virus contains three subunits of prM-E. The virion is not quasi-equivalent, as was found for the mature virus. Each immature spike makes a short helix formed by the distal ends of the E subunits, which are tilted upwards by approximately 25° with respect to the surface and which are only approximately related by a threefold axis (12). The pr domain covers the fusion peptide at the tip of E DII and helps hold the spike together by contacting the other pr domains within a spike (31).

Similar to mature flaviviruses, there is little difference seen in the cryo-EM reconstructions of immature DENV, YFV, ZIKV, and WNV (12, 32, 33). However, the reconstructions of

immature flaviviruses have not reached atomic resolution, so it is difficult to fully evaluate the differences in the viruses. The inability to reach atomic resolution for immature flaviviruses suggests that there is flexibility in immature particles. The glycosylation status of prM is unique for different flaviviruses; glycosylation occurs at N69, N70, and N15 for DENV, ZIKV, and WNV, respectively (15).

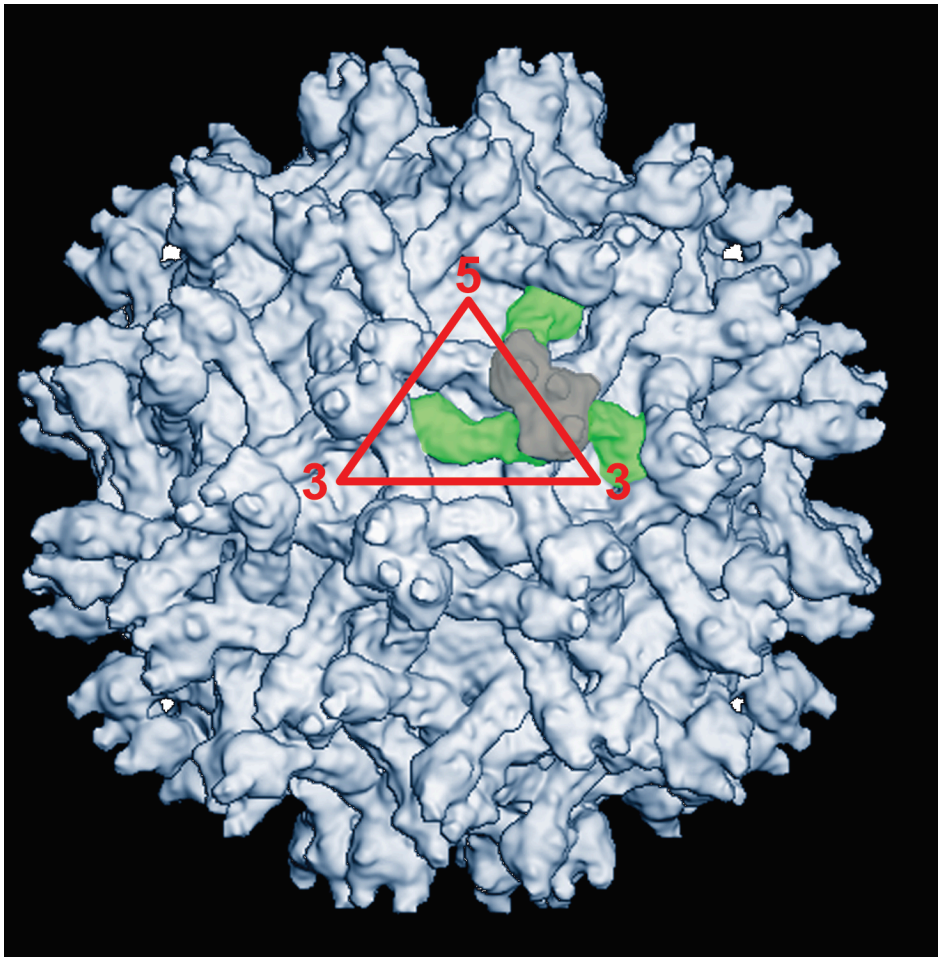

Figure 1.5 Immature flavivirus

Immature flaviviruses have a spiky appearance from the 60 trimeric spikes that decorate the virion surface. The three subunits that make up a spike are indicated in green and gray, for E and prM, respectively. The three prM subunits within the gray density are not individually distinguishable at this resolution. An asymmetric unit is depicted by the red triangle. Adapted with permission from (12).

Unlike in the mature virus where the transmembrane helices of E and M are in close proximity, in the immature virus the transmembrane helices do not make contact and are located farther apart. Therefore, during maturation not only do the ectodomains undergo conformational changes, but a large movement of transmembrane domains also occurs (31). The two M transmembrane helices undergo a rotation with respect to each another during maturation, as in the immature virus they could be fit with an antiparallel coiled coil, whereas in the mature virus each helix had to be fit independently (12, 16). In contrast, E transmembrane helices were readily fit with a coiled coil in both immature and mature cryo-EM reconstructions.

The lipid bilayer is found between 165 and 205 Å radii in both immature virus and mature viruses (28). The membrane has the same polygonal shape in immature virus, with constrictions at local regions where transmembrane helices are present (12). There is a gap of ~30 Å between the inner leaflet of the bilayer and the nucleocapsid core, which is twice the size found in the mature virus. The nucleocapsid core in the immature virus lacks discernable organization, similar to the mature virus (12). However, C fit into weak density observed in the immature ZIKV cryo-EM reconstruction, indicating there may be partial icosahedral symmetry of C (32).

1.5 Dynamics of Flaviviruses

Cryo-EM reconstructions of flaviviruses depict the virus as a static particle, particularly mature virus with its tightly packed arrangement of glycoproteins. However, studies with antibodies and at high temperatures have shown that flaviviruses are dynamic and occupy transient conformational states (Figure 1.6) (34). These transient states, which altogether are termed “viral breathing”, have been studied with antibodies. For example, E111 strongly neutralizes DENV-1, and yet recognizes an epitope that is entirely buried in E DIII (35). Furthermore, three ZIKV-neutralizing antibodies, ZV-2, ZV-48, and ZV-64, recognize a buried epitope in DIII (36).

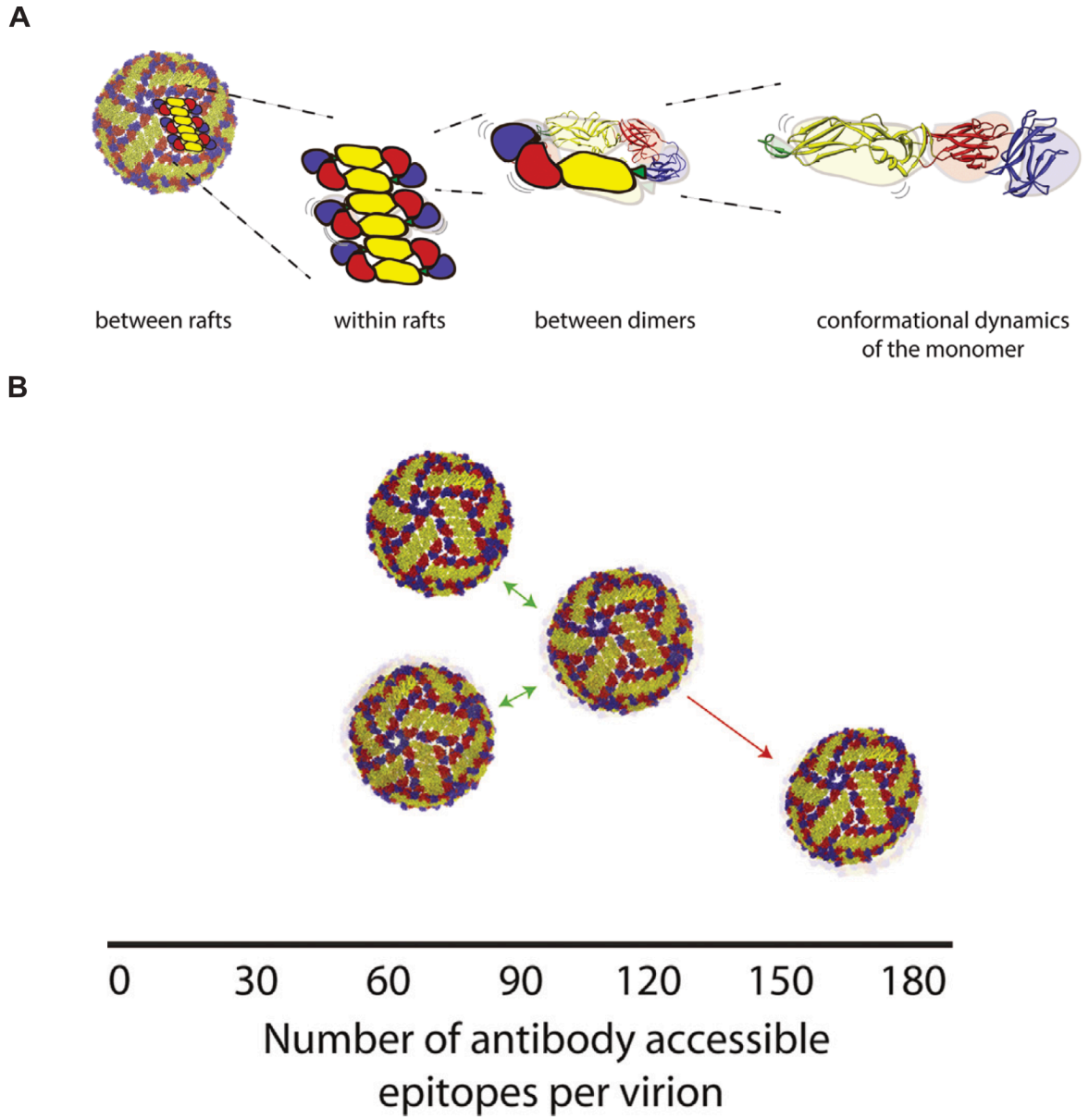

Figure 1.6 Flavivirus conformational dynamics

Flaviviruses exhibit a broad range of motion that influences antibody binding. (**A**) Motion occurs in flaviviruses in-between rafts, within rafts, between dimers, and within E monomers. (**B**) For any epitope, theoretically 180 antibodies can bind to the virus. However, full saturation only occurs after transient epitopes are exposed due to dynamic changes in the virus. Adapted with permission from (34).

Dynamic changes in epitope accessibility were shown to be reversible for both DENV and WNV (37). However, for the neutralizing antibody 1A1D-2 which was shown to bind an

inaccessible region of DIII, it was found that by increasing the incubation temperature to 37°C, the binding of 1A1D-2 to DENV-2 increased from about one-third of particles to nearly all particles (38). This demonstrated that high temperature can influence particle dynamics, which was confirmed by incubating mature DENV-2 at 37°C. The virus had an irreversible "bumpy" phenotype, which was hypothesized to represent a fusion intermediate (39, 40). Neither immature DENV-2, nor mature WNV, was shown to exhibit conformational changes after incubation at 37°C, indicating that mature DENV-2 may transition into a unique dead-end conformation at high temperatures (40, 41).

Heterogeneity in maturation also plays a role in conformational dynamics. Furin processing of flaviviruses is incomplete, yielding partially immature viruses that retain some prM (42). It was found that different cell types produced DENV-2 with varying amounts of prM; virus from dendritic cells, Vero monkey kidney cells, C6/36 insect cells, and HEK 293T kidney cells contained 13, 52, 54, 63% prM, respectively (43). Antibody studies with DIII mAbs have shown that prM content strongly influences neutralization (44, 45). The dynamics of these mixed particles is likely distinct from either fully mature or fully immature particles.

CHAPTER 2. HEAVY-ATOM DERIVATIZATION AND FAB LABELING OF FLAVIVIRUSES TO STUDY MATURATION

2.1 Chapter Summary

Flaviviruses undergo a large structural rearrangement as part of the maturation process. In order to investigate these changes, two strategies were developed including labeling E subunits and trapping maturation intermediates. Labeling was performed by derivatizing immature KUNV with heavy-atom compounds. One candidate, a platinum compound, was found to likely derivatize immature KUNV at prM sites. For trapping studies, the E16 Fab was proposed to trap an intermediate of maturation due to its inaccessible epitope on immature KUNV. In the reconstruction of E16 Fab bound to immature KUNV it was found that E16 bound asymmetrically to one side of the particle, leading to weak distorted density in the reconstruction. These results were inconsistent with the prior assumption that flaviviruses have icosahedral symmetry.

2.2 Introduction

The sequence of events that dictates how flaviviruses transition from immature to mature virions remains unclear. Following the determination of cryo-EM structures for mature and immature flaviviruses, a model was constructed for the conformational rearrangements that occur during maturation by inferring the most probable subunit transitions (46). In this model (Figure 2.1A), the three non-equivalent subunits of prM-E heterodimers are shown in three different colors. Subunits at the fivefold, threefold, and twofold symmetry axis are designated subunits A, B, and C, respectively. During the conformational rearrangement, subunit B was proposed to dimerize with another subunit B from a neighboring asymmetric unit, while subunit A dimerized with

subunit C. The model was based on minimizing the amount of rotation needed for the subunits to dimerize.

An alternative model was constructed by determining high-resolution structures of immature and mature DENV, which allowed for fitting of the stem and transmembrane domains of E and prM/M (31). In this model, subunit C was proposed to dimerize with another subunit C from an adjacent asymmetric unit, while subunit A dimerized with subunit B (Figure 2.1B). The model minimized the amount of translational movement for the stem and transmembrane domains, but included substantial rotation of the subunits up to ~180°. Although the rotation-minimized and the translation-minimized models provide possible pathways for maturation, both models rely on subunit rotations of at least 50°. This would be a reasonable assumption for a virus that is sparsely covered with glycoproteins such as HIV-1, which has only ~14 copies of glycoproteins on its surface (47). However, based on cryo-EM reconstructions, immature flaviviruses are arranged with an icosahedral array of subunits on the virion surface that restricts rotation and translation. Therefore, we aimed here to develop a model that addressed the probable motions of subunits within the context of the virion.

One approach to study the conformational rearrangement of flaviviruses is to trap the virus in an intermediate state using antibodies. The antibody that was selected to trap immature KUNV was E16. E16 mAb was originally isolated by immunizing mice with WNV-NY99 E (48). The antibody was protective against WNV-NY99 challenge in mice, cross-reactive in vitro to 10 different WNV strains, and found to bind to the DIII lateral ridge of E protein (48, 49). E16 Fab binds immature WNV in addition to mature WNV, and E16 Fab was shown to neutralize immature WNV-965 reporter particles (50).

The cryo-EM structure was determined of E16 Fab bound to mature WNV NY99, which showed that E16 bound to only two out of three subunits within an asymmetric unit (51). These were the subunits B and C, located at the threefold and twofold axes, respectively. Steric hindrance blocked potential binding of subunit A at the fivefold. The complex structure provided a model for neutralization, and it was proposed that E16 blocked the conformational rearrangement of E protein during fusion, and therefore, would trap an intermediate state during pH-triggered fusion. A cryo-EM structure of the complex at low pH supported this claim, as it was shown that fusion was inhibited and the virus exhibited membrane expansion and glycoprotein heterogeneity (52). The ability of E16 Fab to differentially label mature virus and trap a fusion intermediate suggest that it can potentially trap an intermediate of maturation.

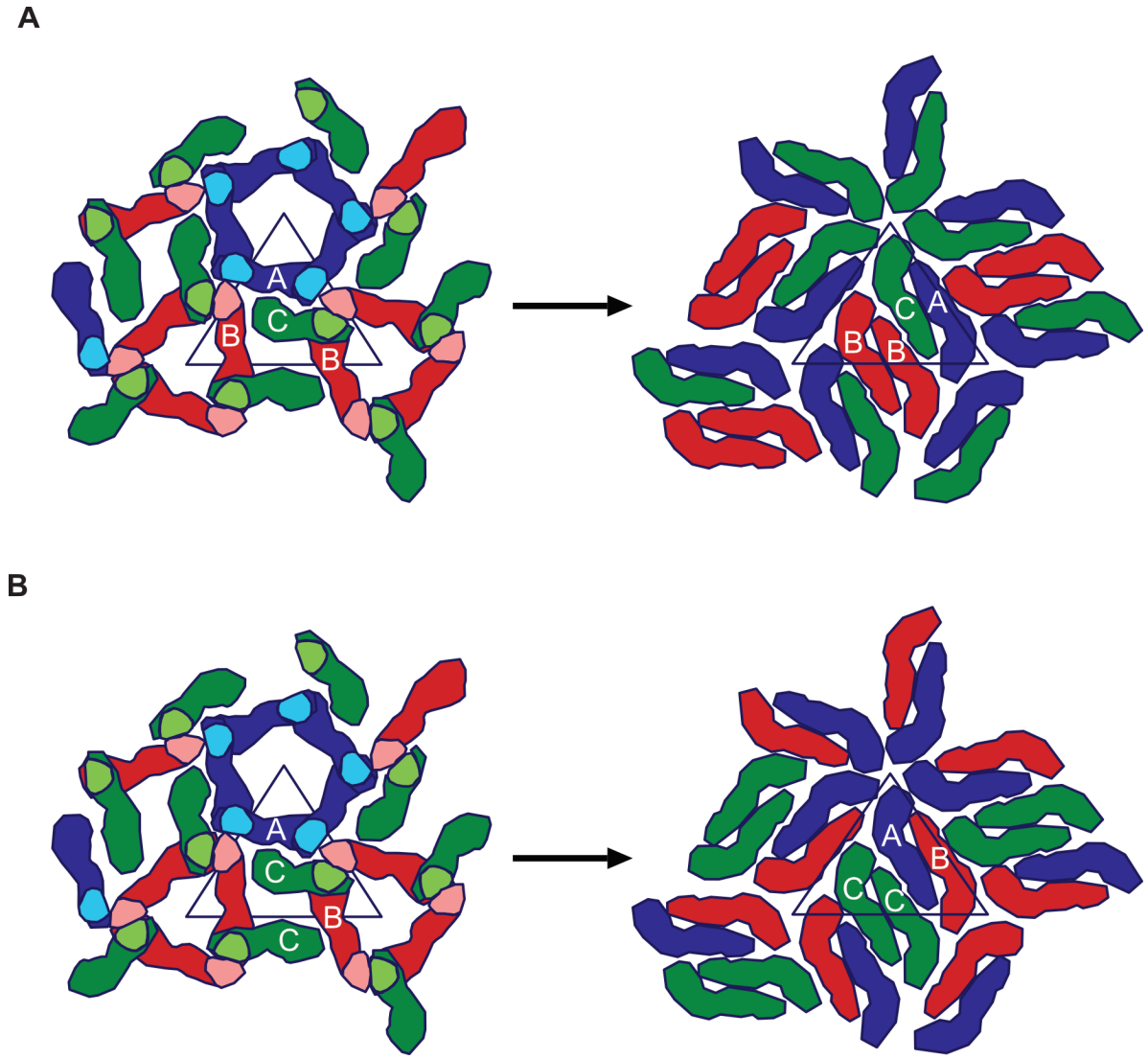

Figure 2.1 Rearrangement of flaviviruses during maturation

Models for the conformational rearrangement of maturation. The arrangement of the three non-equivalent E subunits are shown for the immature virus (left) and the mature virus (right), and colored based on their position in the immature virus. The blue, red, and green subunits are located at the fivefold, threefold, and twofold symmetry axes in the immature virus, respectively. prM is shown in the immature virus as light blue, light red, and light green. An asymmetric unit is depicted by the triangle. (**A**) In this model, subunit B and a neighboring subunit B undergo a large translation and rotate ~150° in order to dimerize at a twofold axis, as subunits A and C dimerize and rotate ~50°. (**B**) An alternative model in which subunit C and an adjacent C undergo a large translation and rotate ~50°, while subunit A and B dimerize by rotating ~140° and ~180°, respectively.

Heavy-atoms derivatives such as platinum and mercury have been used extensively in x-ray crystallography to solve the phase problem (53). Platinum compounds bind to cysteine, histidine, and methionine residues, but have a preference for methionines, while mercury compounds bind to cysteines or histidines, with a preference for cysteines (54). In isomorphous replacement or anomalous scattering the role of heavy atoms is to change the x-ray scattering intensities such that a difference map can be calculated and used to determine protein structure.

In electron microscopy (EM), unlike in x-ray crystallography, image contrast is a major limiting factor. Although scattering by electrons is about 10^4 greater than x-rays, the scattering of different atoms is similar, making it difficult to distinguish sample from background in EM (55). Two common applications of heavy atoms are to increase the visibility of a protein sample with negative staining, or to localize proteins in cells with antibodies conjugated to ~15-nm colloidal gold. In cryo-EM, heavy-atom derivatization of proteins has not found widespread use, but the high electron density of heavy atoms can provide a precise label for a residue or subunit of interest. Examples include the labeling of hepatitis B virus (HBV), groEL, and 2D arrays of integrin beta-1 (56–58). In the case of HBV, it was found that a tetrairidium label was visible at a range of resolutions from 10–25 Å (56). For flaviviruses, due to the non-equivalent chemical environment of subunits within an asymmetric unit, it was hypothesized that each subunit would have a distinct occupancy of a heavy-atom compound.

The maturation process of flaviviruses was studied using both heavy-atom labels and E16 Fab. These experiments led to the hypothesis that the virus did not have perfect icosahedral symmetry, which will be investigated further in Chapter 3.

2.3 Materials and Methods

2.3.1 Cell culture

C6/36 were grown in MEM supplemented with 25 mM HEPES at pH 7.3 and 10% FBS at 30°C.

2.3.2 Virus purification

Purification of immature KUNV was performed as described in Chapter 3, and is reproduced here:

KUNV virus, strain MRM61C, was added to approximately $7x10^7$ C6/36 cells at an MOI of 8 in twenty 150 mm dishes. The passage of the virus was P3, and of the cells was P11. The cells were infected with virus in 5 mL of PBS with 1% FBS, 1% $CaCl_2$ and 1% $MgCl_2$, and rocked for 45 minutes at room temperature, followed by a 15 minute incubation at 30°C. 15 mL of MEM, 25 mM HEPES at pH 7.3 and 2% FBS was added to the cells. The cells were then incubated at 30°C overnight. At 17 hours post infection (hpi), the inoculum was removed, and the cells were washed twice with PBS, and incubated with new media including 20 mM NH_4Cl. The wash and media replacement was repeated at 19 hpi. Virus was harvested at 30, 48, and 70 hpi. Cytopathic effect (CPE) was first observed at 48 hpi.

The 400 mL of media containing virus were clarified at 9,500 RPM in the JA-10 rotor (Beckman Coulter, Inc.) for 20 minutes. 40% (w/v) PEG 8,000 was added to the media to a final concentration of 8%. The media were then stirred slowly at 4°C overnight. The media were spun at 9,500 RPM in a JA-10 rotor (Beckman Coulter, Inc) for 50 minutes. The supernatant was removed and precipitated virus was resuspended in 15 mL of cold TNE pH 8 (12 mM Tris pH 8, 120 mM NaCl, 1 mM EDTA). The virus was then added to a polycarbonate bottle in which 2 mL of a 22% sucrose solution in TNE was underlaid with a Pasteur pipette. The virus was spun in a

Type Ti50.2 rotor (Beckman Coulter, Inc.) at 32,000 RPM for 2 hours. The supernatant was removed and the pellet was resuspended in 1 mL of TNE. A potassium tartrate-glycerol gradient was made with 10%-15%-20%-25%-30%-35% tartrate in TNE in an Ultra-Clear tube (Beckman Coulter, Inc). To make the gradient, 1.5 mL of each layer was overlaid using a 1 mL pipette tip that was cut with scissors to reduce mixing of the layers during layering. The virus was spun for 1 min at 3,000 x g to remove PEG aggregates, and then layered on top of the gradient. The layer interfaces were marked and the gradient was spun for 2 hours at 32,000 RPM in a Type SW-41 rotor (Beckman Coulter, Inc.). The virus was visualized under a blue light. A blue band was observed near the 20%-25% interface, and was extracted with a 22 gauge needle and syringe. The virus was buffer exchanged and concentrated in a 100 kDa concentrator four times with TNE, to a final volume of ~50 μL. Virus purity and the relative concentration of E protein was assessed by SDS-PAGE with BSA standards.

2.3.3 Screening of heavy-atom labels

Solubilized heavy-atom compounds (HR2-442 and HR2-446, Hampton Research) were diluted 1:100 to a concentration of 5 mM in HNE (12 mM HEPES pH 8, 120 mM NaCl, and 1 mM EDTA). Immature KUNV was buffer exchanged into HNE using an 100 kDa concentrator. 3.2 μL of KUNV was added to 0.8 μL of the compound for a final concentration of 1 mM and incubated on ice for ten minutes. The virus-heavy atom mix was run on an 12% SDS-PAGE gel at 170 V, stained with Coomassie Brilliant Blue R-250 and scanned with the Odyssey CLx Imaging System (LI-COR Biosciences). Densitometry analysis was performed with Image Studio Ver 4 (LI-COR Biosciences) by calculating the ratio of band intensities.

2.3.4 Purification of E16 Fab

Humanized E16 IgG was a gift from Michael S. Diamond. E16 Fab was purified using the Pierce Fab Preparation Kit (ThermoScientific), following manufacturer's instructions.

2.3.5 Cryo-electron microscopy

An 0.2 mM final concentration of the Pt-NO_2 compound was added to 2.5 μL immature KUNV and incubated for approximately two minutes. The sample was added to a non-glow discharged ultrathin lacey carbon grid (No. 01824, Ted Pella). The sample was blotted for seven seconds, and then plunge-froze into liquid ethane using an CP3 plunger (Gatan) at 80–90% humidity.

Data was collected using a Talos F200C microscope (Thermo Fisher Scientific) operated at 200 kV and equipped with a Ceta 4k x 4k camera (FEI). 52 images were collected at a defocus of ~10 μm and a dose rate of ~20 $e^-/Å^2$. The magnification used was 45,000X, which corresponded to a pixel size of 3.281 apix.

The E16 Fab-immature KUNV complex was prepared similarly. In brief, fivefold molar excess of E16 Fab was added to immature KUNV at 37°C for 30 minutes, and the sample was added to non-glow discharged lacey carbon grid (No. 01824, Ted Pella), and blotted for six seconds. Data collection on the Titan Krios was performed as described in Chapter 3. A total of 264 cryo-EM movies were collected.

2.3.6 Reconstructions

The icosahedral reconstruction of derivatized immature KUNV was performed as described in Chapter 3, using a beta release of RELION 3.0 (59). In brief, 1,267 "good" particles were chosen from 2D class averages and used for 3D initial model generation. Refinement of the initial model

while imposing icosahedral symmetry converged to 21 Å reconstruction, based on the FSC 0.143 criterion.

Data processing of E16 Fab-immature KUNV was initially performed as described in Chapter 3. In brief, 7,548 "good" particles for E16 Fab-immature KUNV were selected from 2D class averages using a beta release of RELION 2.1 (60). Ab initio model generation, icosahedral reconstructions, and asymmetric reconstructions were performed using cryoSPARC version 2 (61), following the standard refinement procedure. The icosahedral reconstruction did not converge to a consistent solution, while the asymmetric reconstruction reached 22 Å resolution.

2.3.7 Superimposition

The E16-E DIII crystal structure (49) was fit into the cryo-EM structures of immature and mature ZIKV (62, 63) using the program UCSF Chimera (64). E DIII was superimposed onto the density for ZIKV DIII located at a threefold axis.

2.3.8 Heat map

The derivatized immature KUNV map was normalized to the native map by applying the structure factor of native to the derivatized using EMAN2 (65). The derivatized density was then displayed on the native density using UCSF Chimera (64).

2.4 Results

Due to the ability of E16 to trap a fusion intermediate, it was hypothesized that the E16 Fab could also trap an intermediate of maturation. E16 likely trapped a fusion intermediate because it had incomplete occupancy (two out of three subunits) on mature WNV. Therefore, the crystal structure of the E16-E DIII complex (49) was superimposed onto the cryo-EM structure of immature ZIKV in order to predict the occupancy of E16 on immature KUNV (62) (Figure 2.2B).

The superimposition demonstrated that the epitope on immature ZIKV was inaccessible for all three E subunits, as the epitope was blocked by adjacent E proteins in a spike. In contrast, the epitope for E16 was freely accessible on mature ZIKV (63), in agreement with the WNV-E16 complex cryo-EM reconstruction (51). Although the E16 epitope on immature ZIKV appears inaccessible, E16 Fab was shown to neutralize immature WNV-965 reporter particles (50). Therefore, particle flexibility likely plays a role in E16 binding, which support the hypothesis that E16 traps a transient state of the immature virus.

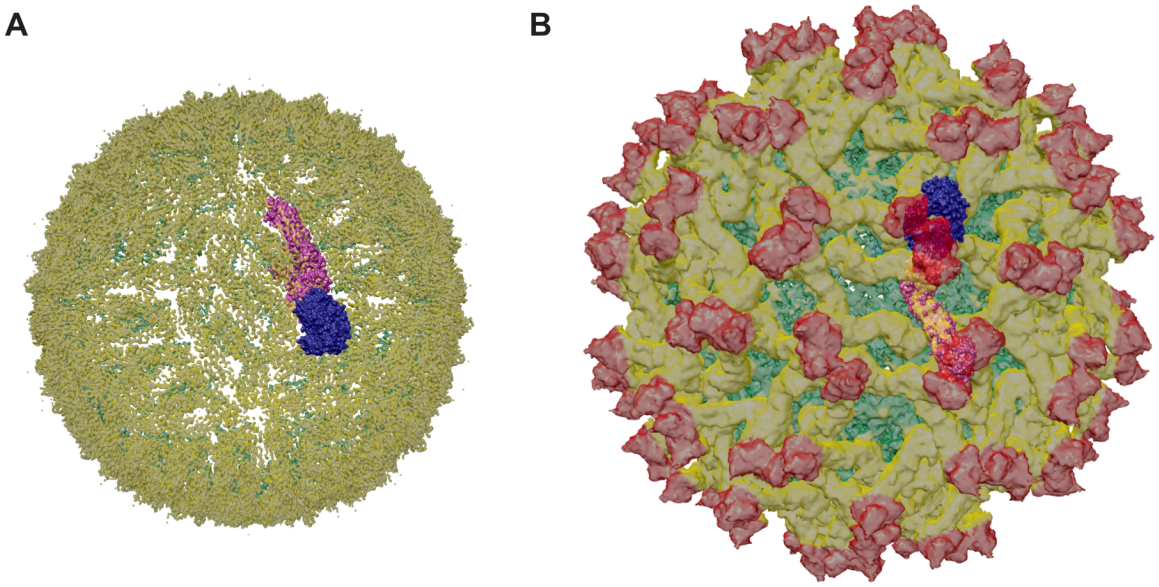

Figure 2.2 E16 epitope accessibility on mature and immature flaviviruses

Semi-transparent surface view of mature and immature ZIKV with superimposed E16-E DIII crystal structure (49). E16 (blue) bound to an E subunit (purple) at the threefold axis was superimposed for both viruses. E16 also clashed with E subunits when superimposed at the fivefold and twofold axes. (**A**) Mature ZIKV (63) and (**B**) immature ZIKV (62).

The ability of heavy atoms to derivatize immature KUNV was also analyzed. Immature KUNV was incubated with heavy-atom compounds which were chosen for derivatization based on their reactivity over a range of pH from 5-8 (Table 2.1) (Hampton Research). pH reactivity was considered because a low pH would be necessary to initiate maturation.

Table 2.1 Properties of heavy-atom compounds used to label immature KUNV

Name	Formula	ID	pH Min	pH Max
Potassium hexachloroplatinate(IV)	K_2PtCl_6	Pt-Cl	4.2	8.4
Potassium tetranitroplatinate(II)	$K_2Pt(NO_2)_4$	Pt-NO_2	2.0	8.6
Potassium tetracyanoplatinate(II) hydrate	$K_2Pt(CN)_4 \cdot xH_2O$	Pt-CN	3.6	8.7
Ethylmercurithiosalicyclic acid, sodium salt	$C_9H_9HgNaO_2S$	Hg	5.4	8.4

The protein and heavy-atom mixtures were screened by SDS-PAGE. A gel shift in the protein bands corresponded to derivatization, although not all derivatized proteins will necessarily show a change in mobility (66). In the gel, both Pt-Cl and the Pt-NO_2 compounds caused E and prM bands to shift in their molecular weight, while neither the Pt-CN nor the Hg compound had this effect (Figure 2.3). For the Pt-Cl compound, smeared bands appeared at ~40 and ~60 kDa, along with a complete loss in intensity of the E band, and an ~85% reduction in the intensity of the prM band, as determined by densitometry analysis compared to mock. For the Pt-NO_2 compound a smear appeared between and 40 and 50 kDa, with an ~82% reduction in the E band intensity and an ~11% reduction of prM intensity. These results indicated that the Pt-Cl and Pt-NO_2 compounds derivatized immature KUNV.

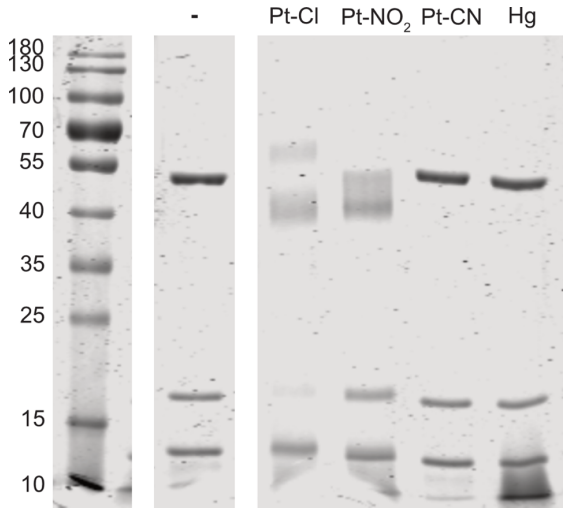

Figure 2.3 Coomassie stained gel of immature KUNV with heavy-atom labels

Immature KUNV was incubated with mock (-), Pt-Cl, Pt-NO_2, Pt-CN, or Hg compounds. The band for E is seen at ~55 kDa, prM ~ 17 kDa, and C ~ 12 kDa.

Cryo-EM datasets were collected on the Titan Krios for native immature KUNV and on the Talos F200C for immature KUNV derivatized with the Pt-NO_2 compound. Heavy-atom derivatization can denature proteins by disturbing protein folding (66). 2D class averages of immature KUNV derivatized with the Pt-NO_2 compound showed that the virus resembled native virus with no obvious defects (Figure 2.4A and B). An icosahedral reconstruction of the ~1,200 particles had the same spiky morphology as immature flaviviruses and reached a resolution of ~21 Å (Figure 2.5).

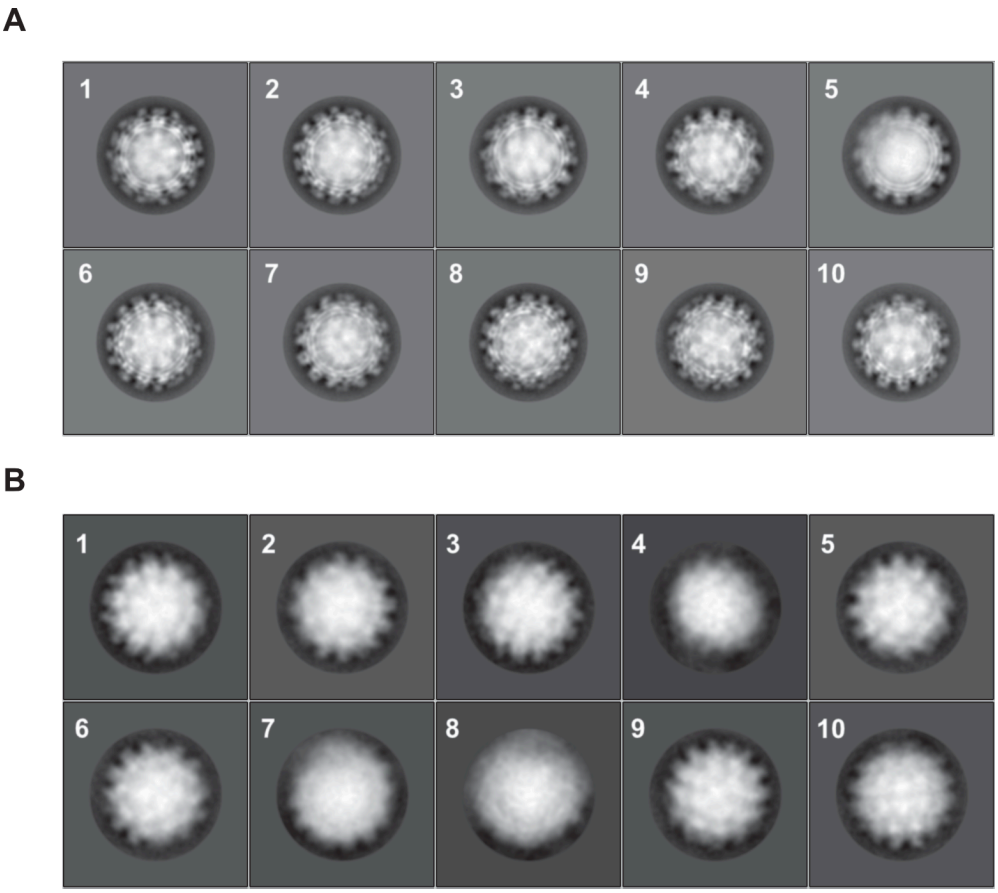

Figure 2.4 2D class averages of immature KUNV datasets

Classes ordered by population for immature KUNV cryo-EM datasets. (**A**) Native immature KUNV. (**B**) Immature KUNV derivatized with the Pt-NO_2 compound.

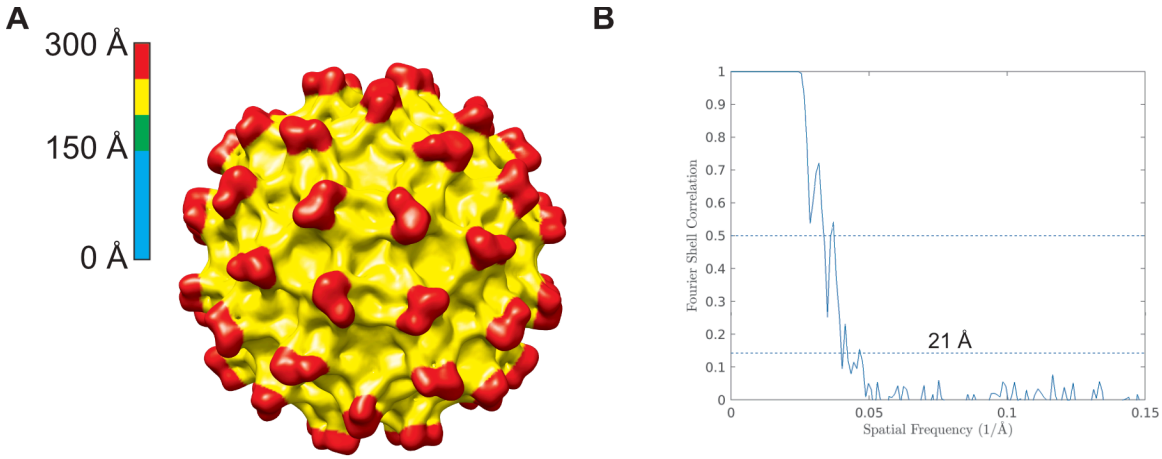

Figure 2.5 Icosahedral reconstruction of derivatized immature KUNV

Cryo-EM reconstruction of immature KUNV derivatized with the Pt-NO_2 compound (**A**) Surface view of the reconstruction contoured at ~3 σ, colored radially as indicated in the color key. (**B**) Fourier shell correlation (FSC) of the reconstruction indicating a resolution of 21 Å based on FSC 0.143 criterion.

Unfortunately, the heavy atoms were not apparent in the 21 Å reconstruction. To identify the possible locations of the heavy atoms, the density of the derivatized reconstruction was normalized to the density of the native reconstruction. The native reconstruction was then colored based on the density of the derivatized reconstruction (Figure 2.6). The highest density differences were found in prM. Based on the known location of the three prM subunits within a spike density, it appears that there is differential labeling with the Pt-NO_2 compound, but a higher resolution structure is required to evaluate this hypothesis.

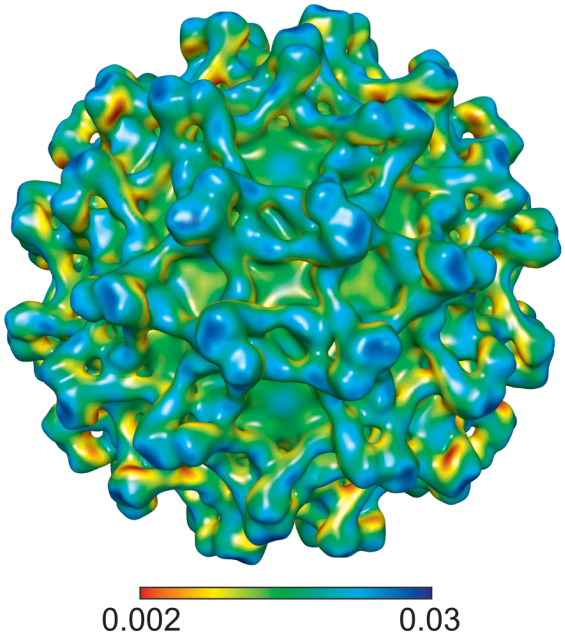

Figure 2.6 Heat map of potential heavy-atom locations

The density of the derivatized reconstruction was normalized to the native virus, and then the native virus was colored based on the density differences, as indicated in the color key. The density values ranged from 0.002 to 0.03. The highest density difference is seen in the prM region of the virus.

A cryo-EM dataset was collected on the Titan Krios for E16 bound to immature KUNV. 2D class averages for E16 bound to KUNV showed no obvious Fab density (Figure 2.7). However, fuzzy density was observed on one side of the particle in almost all classes that extended from the edge of the nucleocapsid core to the glycoprotein layer. Some classes such as 4, 5, 6, 8, and 10 also showed oblong particles, and these particles had cores that appeared to be eccentrically positioned within the glycoprotein layer. Fuzzy density on one side of the particle was also observed in class 5 in native immature KUNV (Figure 2.4A), but it was less apparent than in the Fab-bound complex.

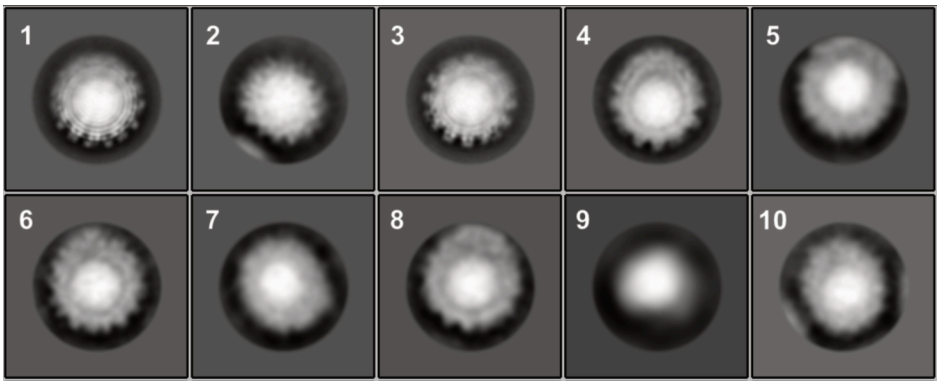

Figure 2.7 2D class averages of the E16 Fab-immature KUNV dataset

Classes ordered by population. Localized fuzzy density in the glycoprotein spikes is most apparent in classes 1 and 3.

An icosahedral reconstruction of the E16 Fab-immature KUNV complex did not converge to a consistent reconstruction. Therefore, an asymmetric reconstruction was performed using cryoSPARC version 2 (61), which resulted in a reconstruction at ~22 Å resolution (Figure 2.8). No density for E16 Fab was seen in this reconstruction. The reconstruction had an overall spiky morphology, characteristic of immature flaviviruses, but weak distorted density was apparent on one side of the particle, in agreement with what was seen in the 2D class averages.

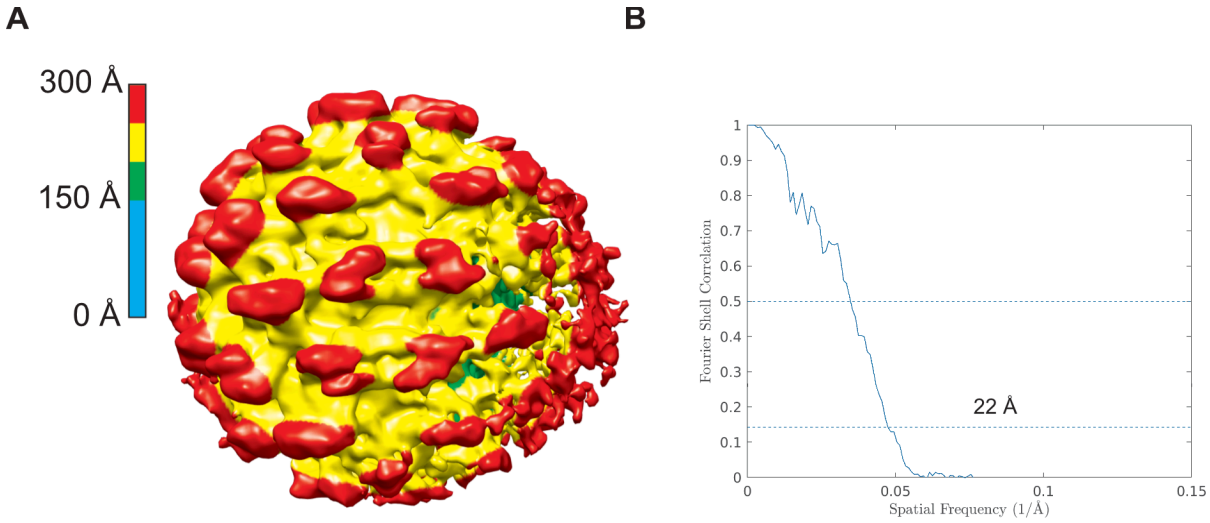

Figure 2.8 Asymmetric reconstruction of E16-immature KUNV complex

(**A**) Surface view of the asymmetric reconstruction of E16-immature KUNV, colored radially as indicated in the color key and contoured at ~2.5 σ. The electron density on one side of the particle is weak and distorted. (**B**) FSC curve indicating that the resolution of the reconstruction is ~22 Å.

A grayscale central cross-section (Figure 2.9), shows the inner density distribution for this reconstruction. Distinct density layers for the inner and outer leaflet of the membrane are apparent in the majority of the membrane. In the weak density region, there are protrusions from the core to the membrane and glycoprotein density layer.

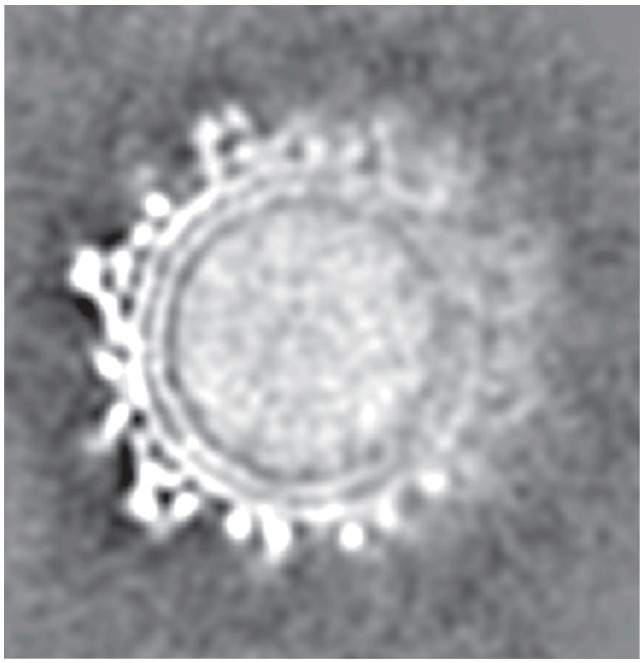

Figure 2.9 Central cross-section for E16 Fab-immature KUNV complex

Grayscale central cross-section for the asymmetric reconstruction. There is weak density on one side of the particle, including protrusions that extend from the core to the membrane layer.

These results indicate that E16 likely binds to a localized flexible region of the virus, and that Fab binding appears to distort the virus and induce heterogeneity.

2.5 Discussion

The conformational rearrangement of flaviviruses was investigated using heavy-atom compounds and E16 Fab. A Pt-NO_2 compound derivatized immature KUNV based on a gel shift assay and a cryo-EM reconstruction of the derivatized virus. After normalizing the density of the derivatized virus to the native virus, it appeared that prM was derivatized by the compound. Further characterization is required to determine if the Pt-NO_2 compound differentially labeled E and/or prM subunits and thus can be used to study maturation.

E16 bound to immature KUNV caused a large change in the structure of the virus, such that when assuming icosahedral symmetry the structure did not converge to a consistent solution. This result was in agreement with the epitope being inaccessible, which was demonstrated by superimposing the crystal structure of E16-E DIII onto the immature virus structure. The asymmetric reconstruction of the complex confirmed that Fab binding led to weak distorted density on one side of the particle.

In both the 2D class averages and the asymmetric reconstruction, there was partial strong density for the glycoprotein spikes at one side of the particle, indicating that E16 must bind to a distinct, localized region of the virus. If instead, virion flexibility was randomly distributed on the virus surface and thus E16 bound randomly, then the averaged reconstruction would have uniformly weak distorted density. This was not observed. Unlike the glycoproteins, the membrane layer and core in the E16-immature KUNV reconstruction appeared generally intact. As is typically observed for flavivirus reconstructions, the core was not well resolved in the reconstruction.

Asymmetric antibody binding of flaviviruses is not limited to E16, as it was shown that ZIKV-195 Fab also bound primarily to one side of mature ZIKV (67). Only 21% of the data was used for the icosahedral reconstruction of the complex because the majority of the 2D class averages displayed a localized binding of the antibody that was too heterogenous to successfully average.

The E16 Fab-immature KUNV reconstruction indicated that immature flaviviruses may have a localized deviation from symmetry. While the E16 Fab was not be usable for probing the sequence of events of flavivirus maturation, it uncovered a false assumption to be investigated in order to understand maturation. Flaviviruses have always been assumed to have icosahedral

symmetry, and the models for maturation were constructed within an asymmetric unit. If flaviviruses assemble with imperfect icosahedral symmetry, the deviations in symmetry would likely impart structural flexibility and facilitate rotations and translations of the E protein subunits. Asymmetry of flaviviruses will be investigated in Chapter 3, with the use of asymmetric reconstructions.

CHAPTER 3. FLAVIVIRUSES HAVE IMPERFECT ICOSAHEDRAL SYMMETRY

The following chapter is a modified version of a publication (68).

3.1 Chapter Summary

Flaviviruses assemble initially in an immature, non-infectious state and undergo extensive conformational rearrangements to generate mature virus. Previous cryo-electron microscopy (cryo-EM) structural studies of flaviviruses assumed icosahedral symmetry and showed the concentric organization of the external glycoprotein shell, the lipid membrane and the internal nucleocapsid core. We show here that when icosahedral symmetry constraints were excluded in calculating the cryo-EM reconstruction of an immature flavivirus, the nucleocapsid core was positioned asymmetrically with respect to the glycoprotein shell. The core was positioned closer to the lipid membrane at the "proximal pole", and at the "distal pole", the outer glycoprotein spikes and inner membrane leaflet were either perturbed or missing. In contrast, in the asymmetric reconstruction of a mature flavivirus, the core was positioned concentric with the glycoprotein shell. The deviations from icosahedral symmetry demonstrated that the core and glycoproteins have varied interactions, which likely promotes viral assembly and budding.

3.2 Introduction

Flavivirus virions mature as they pass through the secretory system, acquiring their membrane when they bud into the endoplasmic reticulum (ER) (69). There are 60 copies of the trimeric glycoproteins present as spikes on the immature virus (31, 32, 46). After exposure to low pH in the trans-Golgi network, the glycoproteins undergo a conformational rearrangement from

60 trimers to 90 dimers, which lie flat on the virus surface (13, 70). In the structures of mature flaviviruses, the glycoproteins are arranged in a herringbone pattern that forms the outer shell of the virus (16, 22, 23, 71, 72). In contrast, flavivirus cores appear to lack a discernable organization, and icosahedrally averaged reconstructions of flaviviruses show no structure for the core other than a roughly spherical shell (16, 22, 23, 29, 31, 32, 46, 71, 72). The crystal and NMR structures of the capsid protein suggest that the capsid associates with genomic RNA on one side and membrane on the other side (30, 73, 74).

Asymmetric cryo-EM reconstructions of bacteriophages have proven useful to elucidate the structure of portals and tails at unique vertices (75, 76). Asymmetric reconstructions have also been used to determine unique features of genomic and protein architecture inside virions (77–82). The antibody reactivity of flaviviruses suggests that virions exhibit conformational variability (34). In order to study unique structural features that may have been hidden by icosahedral averaging, an asymmetric reconstruction was performed of immature Kunjin virus (KUNV), a WNV Australian subtype with low virulence. It was found that the viral core was asymmetrically positioned with respect to the glycoprotein shell. In contrast, an asymmetric reconstruction of mature KUNV showed concentric positioning of the core. However, both structures showed perturbations in the glycoprotein organization.

3.3 Materials and Methods

3.3.1 Cell lines

C6/36 were grown in MEM supplemented with 25 mM HEPES at pH 7.3 and 10% FBS at 30°C. Vero cells were grown in DMEM supplemented with 1X non-essential amino acids (NEAA) and 10% FBS at 37°C.

3.3.2 Immature KUNV infection

KUNV virus, strain MRM61C, was added to approximately $7x10^7$ C6/36 cells at an MOI of 8 in twenty 150 mm dishes. The passage of the virus was P3, and of the cells was P11. The cells were infected with virus in 5 mL of PBS with 1% FBS, 1% $CaCl_2$ and 1% $MgCl_2$, and rocked for 45 minutes at room temperature, followed by a 15 minute incubation at 30°C. 15 mL of MEM, 25 mM HEPES at pH 7.3 and 2% FBS was added to the cells. The cells were then incubated at 30°C overnight. At 17 hours post infection (hpi), the inoculum was removed, and the cells were washed twice with PBS, and incubated with new media including 20 mM NH_4Cl. The wash and media replacement was repeated at 19 hpi. Virus was harvested at 30, 48, and 70 hpi. Cytopathic effect (CPE) was first observed at 48 hpi.

3.3.3 Mature KUNV infection

Approximately $1x10^7$ Vero cells at P11 were infected by KUNV virus P3 at an MOI of 8. The cells were infected as described for immature virus, with the following changes: incubations were performed at 37°C and the media used during the infection was DMEM with 1X NEAA and 2% FBS. Virus was harvested at 24, 50 and 70 hpi, and CPE was first observed at 24 hpi.

3.3.4 Virus purification

The 400 mL of media containing virus were clarified at 9,500 RPM in the JA-10 rotor (Beckman Coulter, Inc.) for 20 minutes. 40% (w/v) PEG 8,000 was added to the media to a final concentration of 8%. The media were then stirred slowly at 4°C overnight. The media were spun at 9,500 RPM in a JA-10 rotor (Beckman Coulter, Inc) for 50 minutes. The supernatant was removed and precipitated virus was resuspended in 15 mL of cold TNE pH 8 (12 mM Tris pH 8, 120 mM NaCl, 1 mM EDTA). The virus was then added to a polycarbonate bottle in which 2 mL of a 22% sucrose solution in TNE was underlaid with a Pasteur pipette. The virus was spun in a

Type Ti50.2 rotor (Beckman Coulter, Inc.) at 32,000 RPM for 2 hours. The supernatant was removed and the pellet was resuspended in 1 mL of TNE. A potassium tartrate – glycerol gradient was made with 10%-15%-20%-25%-30%-35% tartrate in TNE in an Ultra-Clear tube (Beckman Coulter, Inc). To make the gradient, 1.5 mL of each layer was overlaid using a 1 mL pipette tip that was cut with scissors to reduce mixing of the layers during layering. The virus was spun for 1 min at 3,000 x g to remove PEG aggregates, and then layered on top of the gradient. The layer interfaces were marked and the gradient was spun for 2 hours at 32,000 RPM in a Type SW-41 rotor (Beckman Coulter, Inc.). The virus was visualized under a blue light. A blue band was observed near the 20%/25% interface, and was extracted with a 22 gauge needle and syringe. The virus was buffer exchanged and concentrated in a 100 kDa concentrator four times with TNE, to a final volume of ~50 µL. Virus purity and the relative concentration of E protein was assessed by SDS-PAGE with BSA standards.

3.3.5 Cryo-electron microscopy

2.5 µL of virus was added to the carbon side of non-glow discharged ultrathin lacey carbon grids No. 01824 (Ted Pella) and plunge-frozen into liquid ethane using an CP3 plunger (Gatan) at 85% humidity. Blotting times used were between 6 and 8 seconds.

Data was collected using a Titan Krios microscope (FEI) operated at 300 kV and equipped with a K2 Summit direct electron detector (Gatan). The magnification used was 18,000X in super-resolution counting mode, which corresponded to a pixel size of 0.81 Å per pixel. The objective lens astigmatism was corrected with s2stigmator (83). Frames were recorded every 0.2 s for 8 s, with a dose rate of ~ 8 electrons per physical pixel per second. The total dose for each image stack of forty frames was ~ 24 electrons per $Å^2$. The defocus range used was -0.5 to -3 µm.

387 and 369 movies were collected for immature and mature virus, respectively. The Appion (84) and Leginon (85) systems were used for data collection and preprocessing. Individual frames of raw movies were aligned and distortion corrected with MotionCor2 (86). CTF values were estimated with CTFFIND4 (87). Particle picking was done with FindEM (88), resulting in 12,567 immature particles and 23,145 mature particles. A box size of 1280 x 1280 pixels was used for both particles, and the particles were binned 4x.

3.3.6 Icosahedral reconstruction

Reconstructions were performed with a beta release of the RELION 2.1 program (60). For the immature virus reconstruction, a particle mask of 650 Å in diameter was used. Two rounds of 2D alignment and classification were performed to remove "junk" particles from the dataset. The first round was run with 50 classes. Fifteen "good" classes were selected, which contained a total of 9,368 particles. A second round of 2D classification with 40 classes was run. Ten classes contained particles with defined features, which in total contained 7,396 particles. A random subset of 2,000 particles were selected from this dataset for initial model generation.

Five iterations of stochastic gradient descent (SGD) were performed in RELION with the 2,000 particle subset to generate an initial model. Two rounds of refinement of the initial model were then performed using "auto-refinement" mode, which was run with all 7,396 particles while icosahedral symmetry was imposed. Sampling was initiated with 3.75° global sampling and local sampling starting at 0.9°. The reconstruction reached 9.3 Å using the "gold-standard" Fourier shell correlation (FSC) of 0.143.

The reconstruction for mature virus was performed similarly. A particle mask of 550 Å in diameter was used for the mature particle. Two rounds of 2D classification were performed to remove "junk" particles. In the first round, 50 classes were used, and eleven classes were selected

that contained 16,938 particles. A second round of 2D classification resulted in two major classes that that were selected with a total of 9,206 particles. The particle set was used for SGD initial model generation in RELION. Refinement was carried out in “auto-refinement” mode, using the initial model low-pass filtered to 80 Å. The resolution was estimated to be 6.4 Å using the “gold-standard” FSC.

3.3.7 Asymmetric reconstruction

Asymmetric reconstructions were performed with RELION 2.1. The icosahedral reconstruction of the immature virus was used as an initial model and low-pass filtered to 35 Å. Sampling was initiated with 3.75° global sampling and local sampling starting at 0.9°. The angles for the 9,368 particles used in the icosahedral reconstruction were matched to the icosahedral density without imposing symmetry. As the map is icosahedral it would not be expected to change greatly, as each of the 60 icosahedral positions are equally valid for a given image. However, the nucleocapsid core repositioned itself from the center to one side of the glycoprotein shell within five iterations, which suggests its signal was strong enough to select a unique orientation. The reconstruction reached 19 Å resolution.

The refinement was repeated in “3D classification” mode, with a T factor of 0.5. A low T factor was suggested to promote the emergence of asymmetric features in the refinement of other viruses (81). This structure also resulted in the same asymmetric positioning of the nucleocapsid core.

Mature virus was reconstructed using the icosahedral mature virus, low pass filtered to 40 Å resolution, as an initial model. The refinement, using 9,206 particles, reached 35 Å resolution. The asymmetric reconstruction of immature KUNV likely reached higher resolution because the

immature virus has recognizable “spiky” features as compared to the smooth surface of the mature virus, which made alignment more accurate for the immature virus.

3.3.8 Asymmetric reconstruction of immature ZIKV

An asymmetric reconstruction was calculated for immature ZIKV using previously published data (32). The reconstruction was performed using the standard refinement procedure in cryoSPARC (61), and reached ~20 Å resolution. Similar to the immature KUNV reconstruction, asymmetric features such as the eccentric positioning of the core were observed in the immature ZIKV reconstruction.

3.3.9 Simulations

To validate the asymmetric reconstruction method, simulations were performed with RELION. The icosahedral reconstruction of immature KUNV was projected using “relion_project” for the 7,396 orientations determined for the icosahedral reconstruction. Noise was added to the simulated projections. The simulated projections were then used to refine the icosahedral reconstruction, without imposing symmetry. The reconstruction maintained its icosahedral symmetry and did not have an eccentrically positioned core. Thus, the reconstruction procedure did not introduce asymmetrical artifact.

A similar simulation was performed to confirm that known asymmetry was properly aligned and averaged during the asymmetric reconstruction. The asymmetric reconstruction of immature KUNV was projected at the orientations determined for the asymmetric reconstruction, and noise was added. The asymmetric refinement of an icosahedral initial model led to the emergence of features observed for the asymmetric reconstruction within five iterations.

3.3.10 Image generation, local resolution estimates, and measurements

Immature and mature reconstructions were contoured at 3 σ in UCSF Chimera (64). Local resolution maps of immature KUNV were generated using ResMap (89) with a maximum resolution of 12 Å for the icosahedral reconstruction, and 45 Å for the asymmetric reconstruction. JSPR (90) was used to calculate radial density distributions. Figures were prepared with UCSF Chimera and Affinity Designer (Serif). UCSF Chimera and IMOD (91) were used to perform measurements of the particles.

3.4 Results

Cryo-EM movies of immature and mature KUNV were collected on an FEI Titan Krios equipped with a K2 direct electron detector (Table 3.1). Immature and mature KUNV showed characteristic "spiky" particles and "smooth" particles, respectively (Figure 3.1). An asymmetric reconstruction of immature KUNV was performed with the program RELION 2.1 (60), starting with an icosahedral reconstruction (Figure 3.2A and B) as an initial model. The asymmetric reconstruction was refined to ~20 Å resolution (Figure 3.2C and D and 3.3).

Table 3.1 Cryo-EM data collection and processing statistics

Dataset	Immature KUNV	Mature KUNV
Microscope	Titan Krios	Titan Krios
Accelerating voltage, kV	300	300
Camera	Gatan K2	Gatan K2
Mode	Super-resolution	Super-resolution
Number of movies	387	369
Pixel size, Å/pixel	0.81	0.81
Dose rate, e^-/pixel/s	8	8
Total dose $e^-/Å^2$	24	24
Frame rate, ms	200	200
Defocus, mm	0.5-3.0	0.5-3.0
Number of particles for reconstruction	7,396	9,206
Icosahedral resolution, Å	9.3	6.4
Asymmetric resolution, Å	19	35

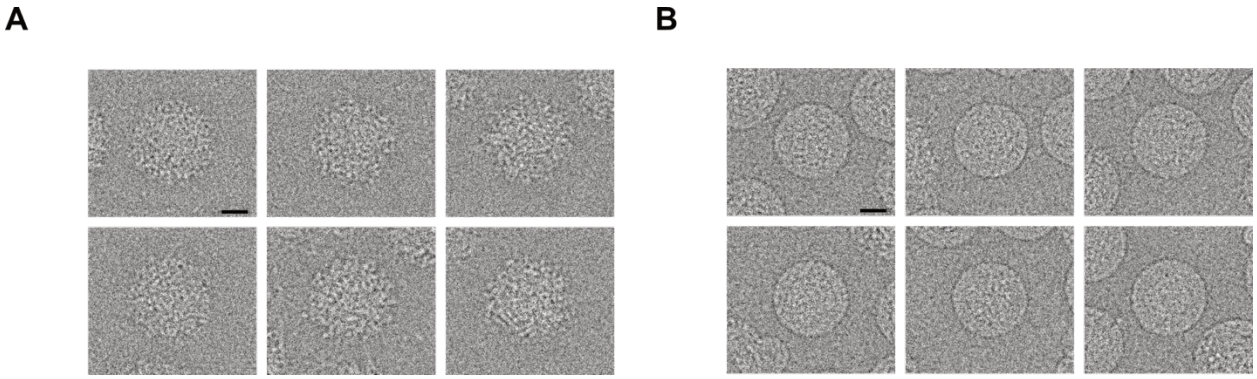

Figure 3.1 Cryo-EM particles of immature and mature KUNV

Particles from cryo-EM micrographs of (**A**) immature "spiky" KUNV and (**B**) mature "smooth" KUNV. The defocus for these particles was 2-3 μm. Scale bar is 200 Å.

The position of the majority of the glycoprotein trimers in the asymmetric reconstruction of the immature virus correspond to their position in the icosahedral reconstruction, demonstrating that the glycoprotein shell has approximate icosahedral symmetry. In addition, the position of the transmembrane densities of these glycoproteins in the asymmetric reconstruction is essentially the same as in the icosahedral reconstruction.

However, unlike the icosahedral reconstruction in which the nucleocapsid core density is situated concentric with the glycoprotein shell, in the asymmetric reconstruction the nucleocapsid core is positioned eccentrically, coming closer to the membrane on one side, the "proximal pole", than on the other side, the "distal pole", of the glycoprotein shell. At the distal pole, where the core is farthest from the glycoprotein shell, there are significant distortions in the glycoprotein organization (Figure 3.2D). The poles are defined by a line that passes through the center of the reconstruction and intersects the approximate center of the distorted glycoprotein density in the asymmetric reconstruction (Figure 3.2E).

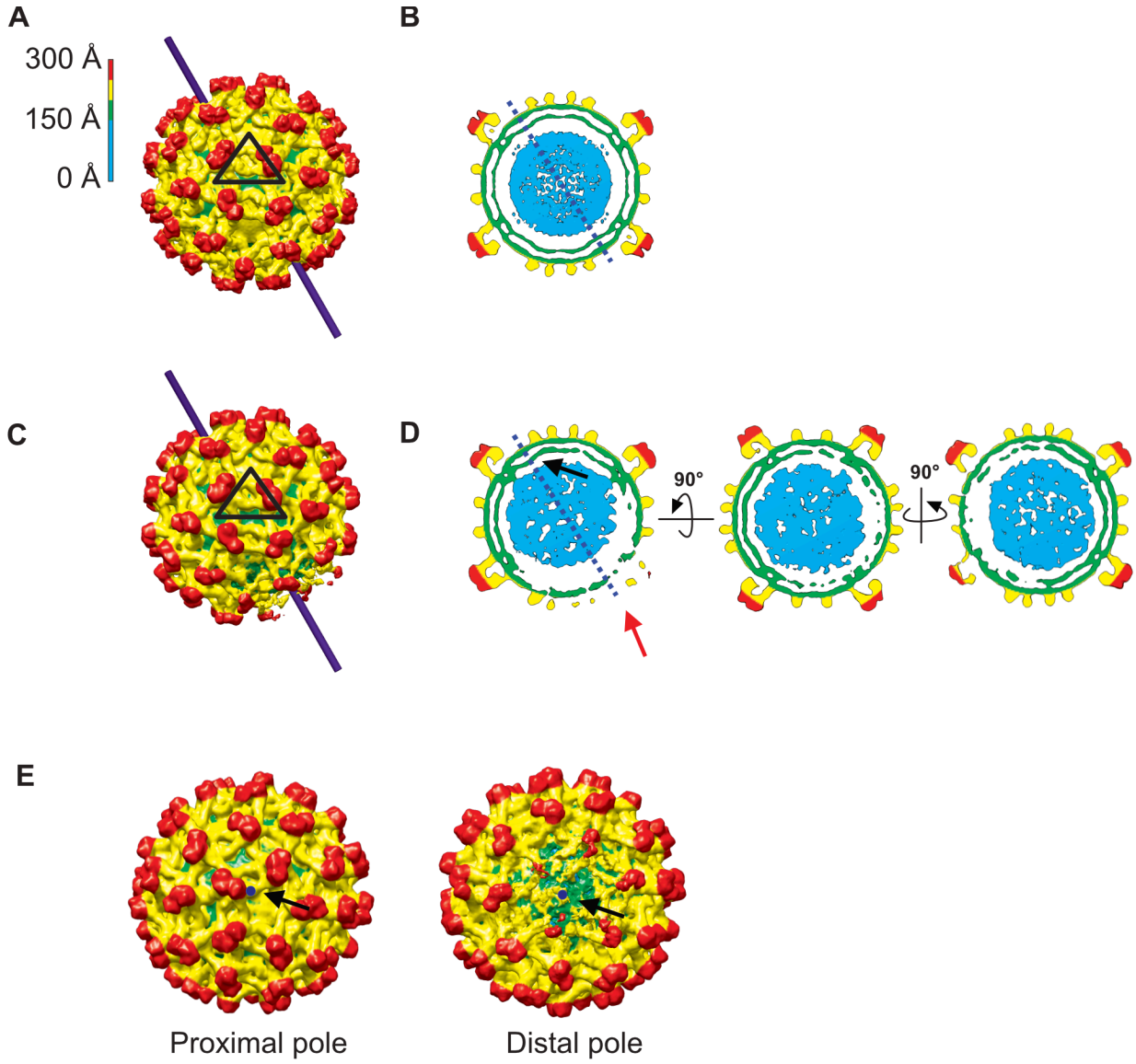

Figure 3.2 Cryo-EM reconstructions of immature KUNV

(**A**) Surface view of the icosahedral reconstruction, colored radially as indicated in the color key. The icosahedral asymmetric unit is indicated by a black triangle. (**B**) Central cross-section of the icosahedral reconstruction. (**C**) Surface view of the asymmetric reconstruction. (**D**) Central cross-section of the asymmetric reconstruction shown in three orthogonal views. The black arrow indicates the proximal pole, where the nucleocapsid core approaches closer to the glycoprotein shell, whereas the red arrow indicates the distal pole, where the core is farthest from the shell. The solid line in **A** and **C** and the dotted line in **B** and **D** are defined by joining the points of the center of the reconstruction and the approximate center of the glycoprotein distorted density in the asymmetric reconstruction. (**E**) Surface view of the asymmetric reconstruction showing the locations of the proximal and distal poles. Black arrows point to where the solid line intersects the glycoprotein surface. All reconstructions are contoured at 2-3 σ.

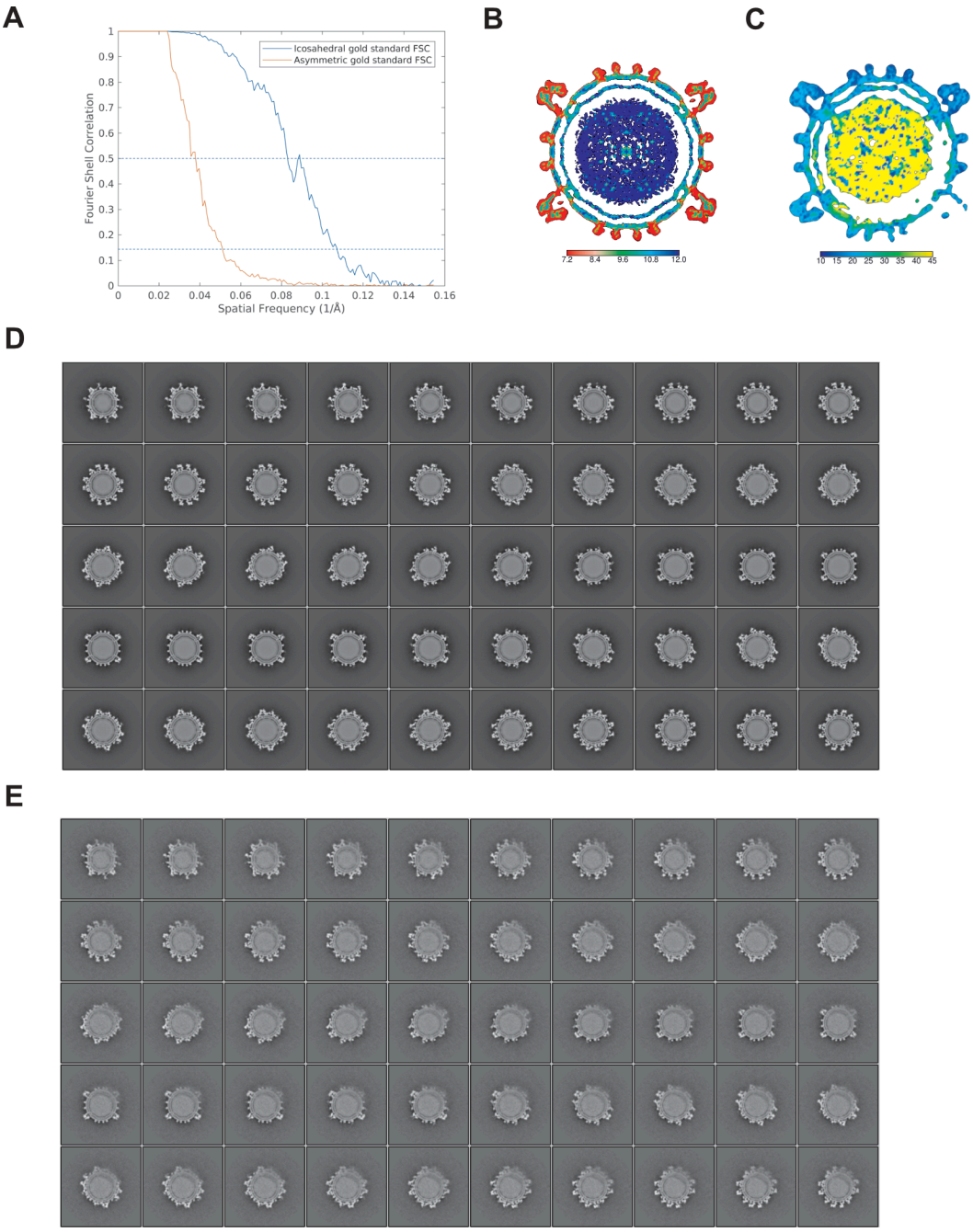

Figure 3.3 Characterization of immature KUNV reconstruction

(**A**) FSC curves of two random half-sets of icosahedral (blue) and asymmetric (red) reconstructions. (**B**) Central cross-section of the icosahedral reconstruction colored by local resolution. (**C**) Central cross-section of the asymmetric reconstruction colored by local resolution. Grayscale sections of (**D**) icosahedral and (**E**) asymmetric reconstructions.

The eccentricity of the core was also observed in an independent asymmetric reconstruction of immature ZIKV (Figure 3.4A and B). Furthermore, a test was performed to validate that the method was unbiased: simulated projection images were generated from an icosahedral reconstruction of immature KUNV, which were then used for a reconstruction without imposing symmetry. The reconstruction was icosahedral, demonstrating that relaxing symmetry constraints during a reconstruction did not induce artificial asymmetry (Figure 3.4C).

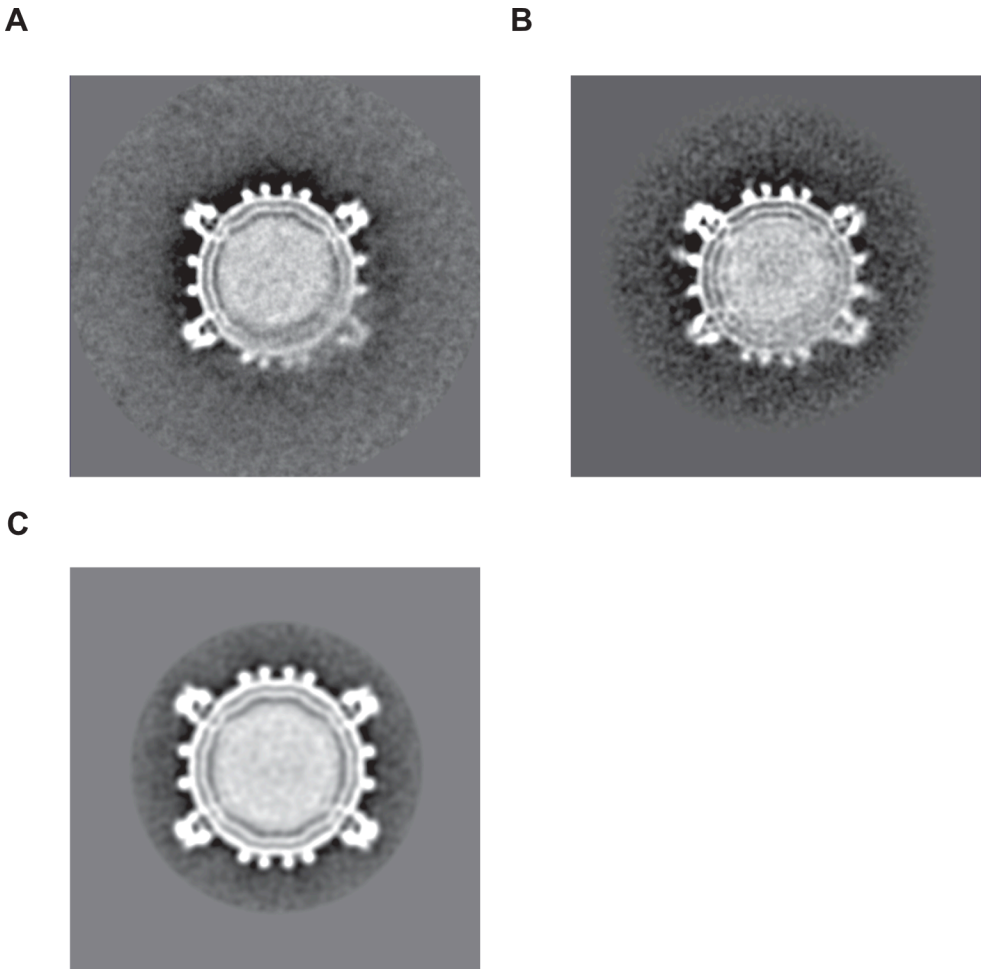

Figure 3.4 Asymmetric reconstructions

Grayscale central sections of reconstructions. (**A**) Immature KUNV reconstruction. (**B**) Immature ZIKV reconstruction. (**C**) Simulated icosahedral data.

The core density in the asymmetric reconstruction is an oblate spheroid, with an approximate diameter of ~260 Å stretching from pole-to-pole (Figure 3.5). The gap between the core and the inner leaflet of the membrane is ~23 Å at the proximal pole, slightly smaller than the gap observed in the icosahedral reconstruction. The maximum external diameter of the glycoprotein shell is ~560 Å. There are density protrusions from the core connecting it to density that represents presumably transmembrane helices of the prM and E glycoproteins.

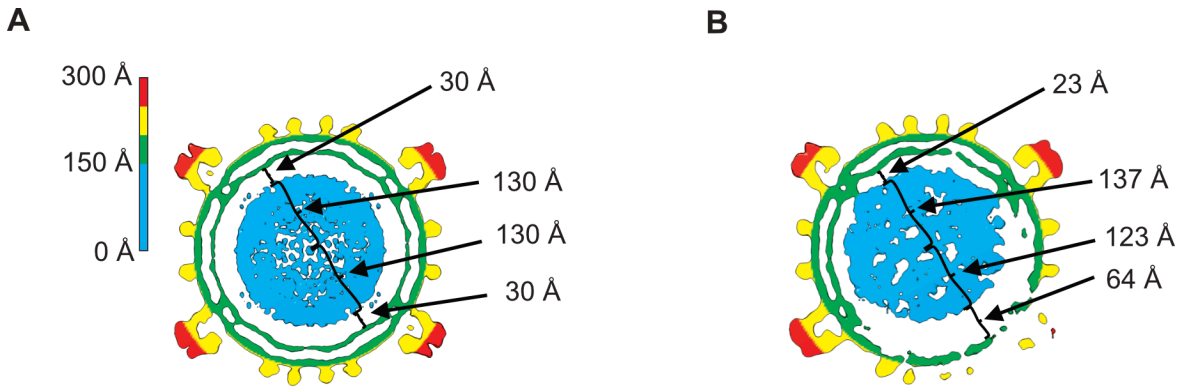

Figure 3.5 Measurements of immature KUNV

(**A**) Central cross-section of the icosahedral reconstruction colored radially as indicated in the color key. (**B**) Central cross-section of the asymmetric reconstruction. Reconstructions are contoured at 3 σ, and arrows indicate distances defined by the brackets.

Density for the inner leaflet of the membrane and the transmembrane helices is missing in the distal pole region, resulting in a large gap between the core and membrane of ~64 Å. A radial density plot shows there is a density peak at the distal pole, near the expected radius for the inner leaflet, which is not observed at the proximal pole (Figure 3.6). This suggests there is distinct density at the distal pole region.

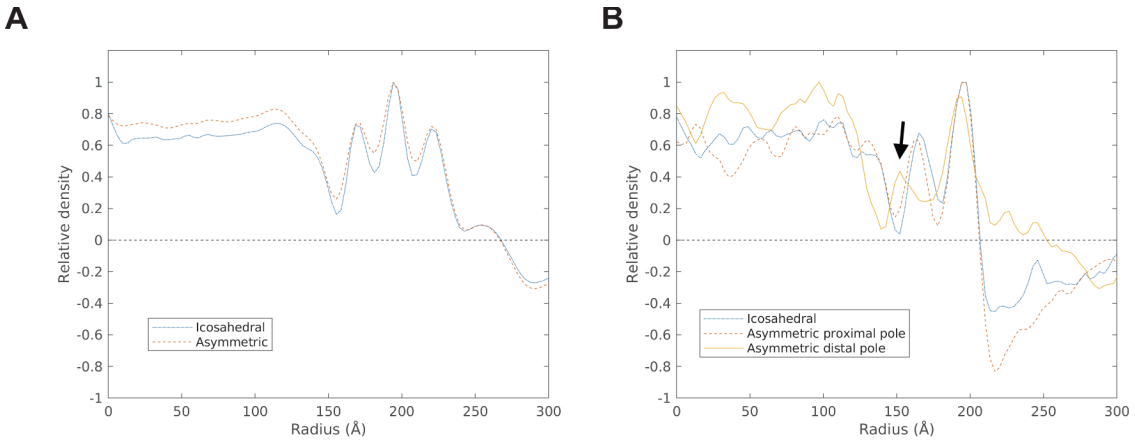

Figure 3.6 Comparison of density values in immature KUNV reconstructions

(**A**) Radial density plot of rotationally averaged icosahedral and asymmetric reconstructions. The center of the asymmetric reconstruction was defined by aligning the reconstruction to the icosahedral reconstruction. The icosahedral and asymmetric reconstructions are shown in blue and red, respectively. (**B**) Radial density plots calculated in the direction of a fivefold axis. The icosahedral reconstruction was rotated so that a fivefold axis was positioned along the Z-axis in Chimera. The asymmetric reconstruction was aligned to the icosahedral reconstruction, by aligning the fivefold axis closest to either the proximal pole or distal pole to the icosahedral fivefold axis positioned on the Z-axis. The icosahedral radial density plot is shown in blue, and asymmetric radial density plots for the proximal pole and distal pole are shown in red and yellow, respectively. The asymmetric distal and proximal pole share density features such as a peak at ~195 Å for the outer leaflet of the membrane. However, the asymmetric distal pole has a distinct density distribution, such as the peak at ~150 Å (black arrow) that is not observed in the icosahedral reconstruction or at the proximal pole of the asymmetric reconstruction.

A ~35 Å asymmetric reconstruction of mature KUNV was calculated using an icosahedral reconstruction as an initial model (Figure 3.7). This reconstruction has layers of membrane and glycoproteins at the same radial distance as in the icosahedral reconstruction. The virus is roughly spherical, and has an uneven surface, with a large patch of distorted density. The core in the asymmetric reconstruction of the mature virus (unlike in the immature virus) is positioned concentric with the glycoprotein shell (Figure 3.7D). Protrusions extend from the core in the mature virus into the glycoprotein layer, but the density is noisy, and less well resolved than for the immature virus.

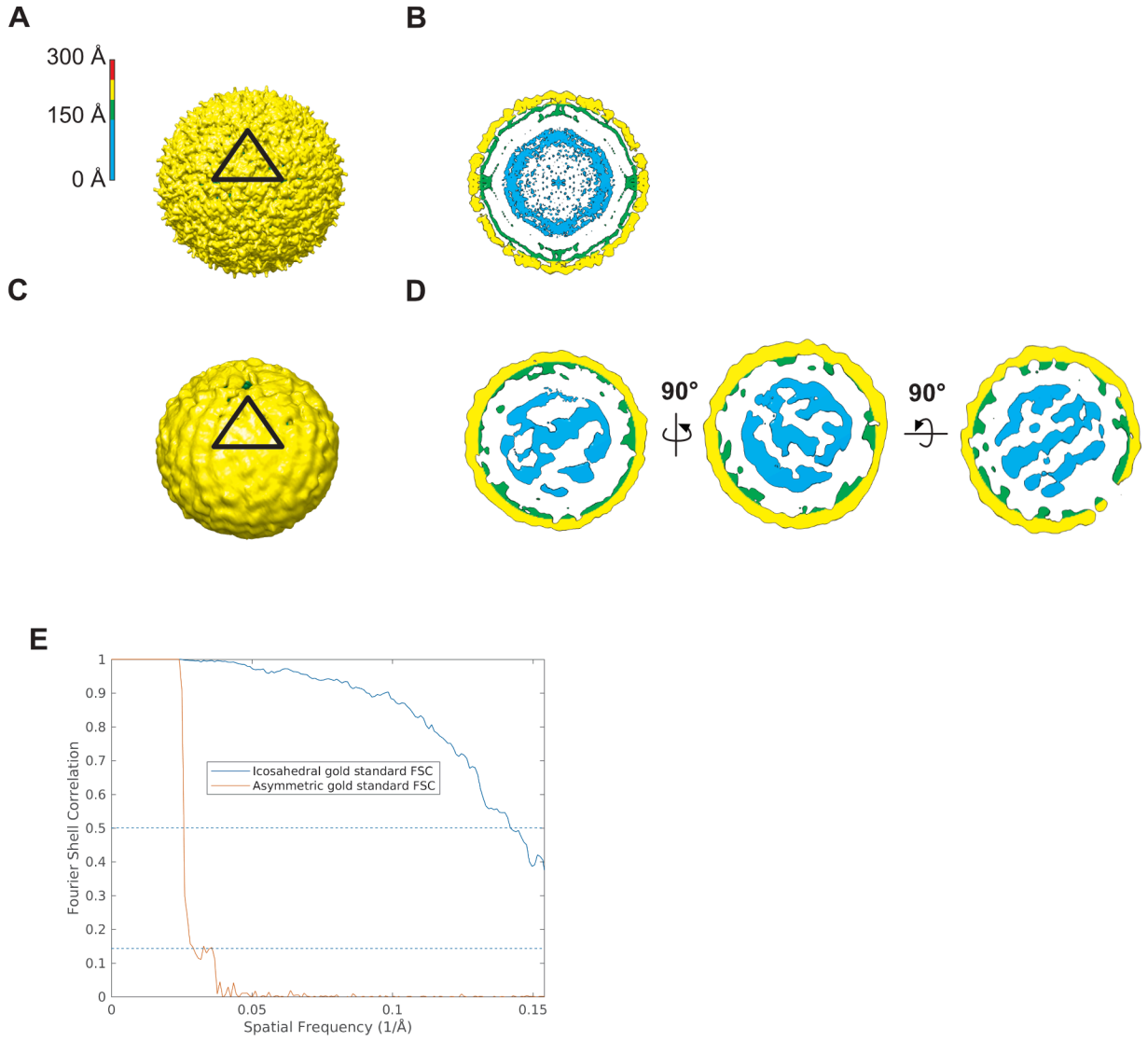

Figure 3.7 Cryo-EM reconstructions of mature KUNV

(**A**) Icosahedral reconstruction of mature virus colored radially as indicated by the color key with the asymmetric unit indicated by a black triangle. (**B**) Cross-section of the icosahedral reconstruction. (**C**) Asymmetric reconstruction of the mature virus. (**D**) Cross-sections of the asymmetric reconstruction shown in three orthogonal views. All reconstructions are contoured at ~3 σ. (**E**) FSC curves of two random halfsets of the icosahedral (blue) and asymmetric (red) reconstructions. The icosahedral reconstruction reached the Nyquist frequency at a pixel size of 3.24 Å/pixel (4x binned).

3.5 Discussion

Cells infected with a flavivirus synthesize glycoproteins that probably form trimers in the membranes of the endoplasmic reticulum. As these trimers aggregate in the ER membrane, each with essentially the same structure and in identical environments, they will tend to form icosahedral structures as predicted for the assembly of viruses by Crick and Watson (92). However, what determines the triangulation number and size of the final assembled virus is unclear. One determinant that may influence particle size is the nucleocapsid core. In the absence of a core, recombinant subviral particles (SVPs) containing prM and E have been reported to have a triangulation number of T=1 (93). The core in immature KUNV contacts the glycoproteins at their transmembrane domains, as was also observed for immature ZIKV (32), and these interactions could influence particle assembly and size. There are likely multiple determinants of particle size, since SVPs lacking cores have been observed that separate into two distinct size classes of approximately the same size as infectious virions as well as the smaller T=1 predicted particles (94).

The tendency to form three-dimensional icosahedral structures of any size in a membrane is inconsistent with the normal planar structure of a membrane. As more trimeric glycoproteins are recruited into the nascent icosahedral structure, there is pressure for the partially formed glycoprotein shell to grow and finally close at what will become the distal pole (Figure 3.8). The closing of the shell is likely impeded by the high membrane curvature and steric clashes with adjacent spike glycoproteins at the bud neck, and probably results in missing trimers at the distal pole. In agreement with this hypothesis, a simulation of icosahedral virus budding determined that the final 1-3 subunits were not incorporated into nascent particles (95). Alternatively, one or more host proteins that might promote budding could be incorporated into the virus particle at the late stage of viral budding. It is unknown what viral and host machinery is involved in membrane

scission during the final moments of budding, but the ESCRT proteins may play a role, as these were implicated for flavivirus budding (96).

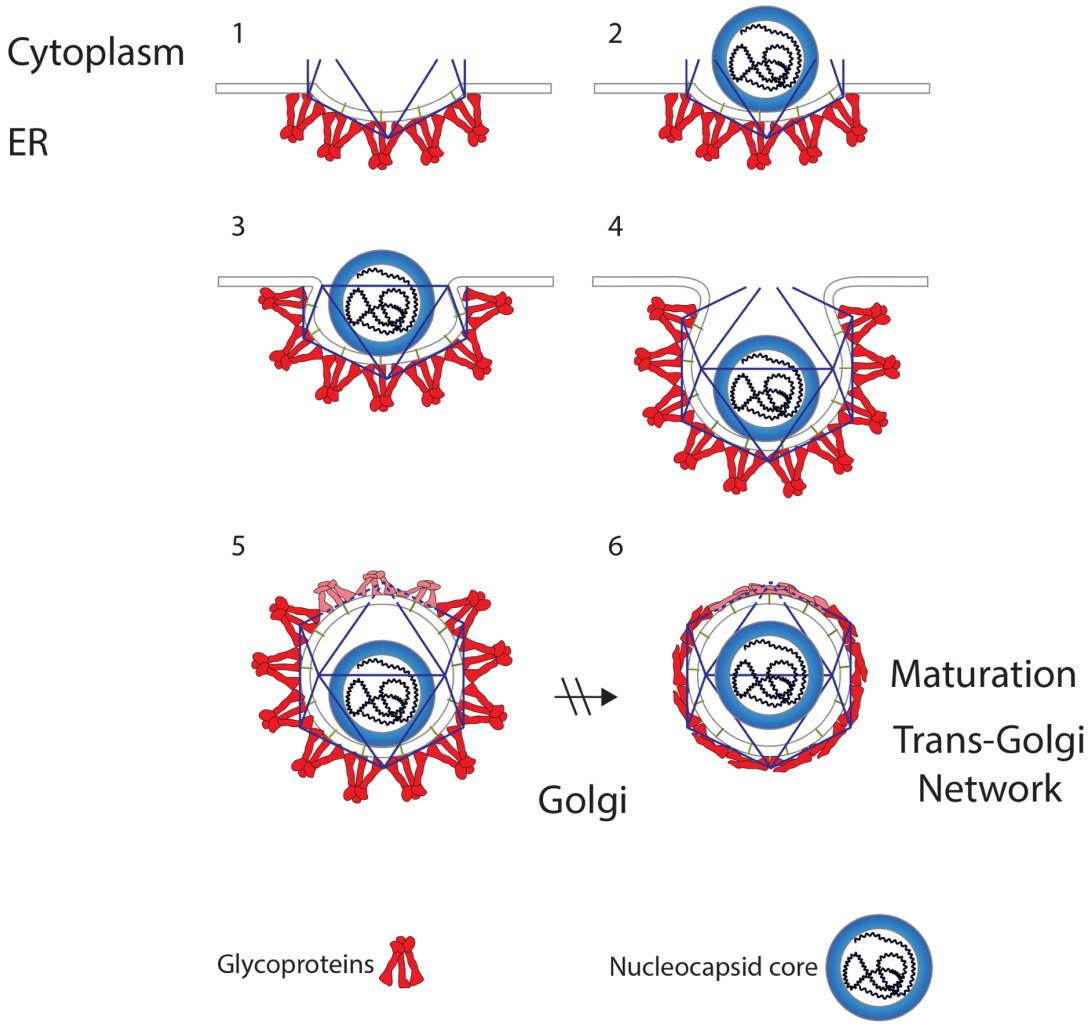

Figure 3.8 Model for flavivirus assembly

(1) The glycoproteins (red) assemble on the ER membrane and form the beginning of an icosahedron. (2) The nucleocapsid core (blue), which has an unknown structure, interacts with the glycoproteins on the ER membrane. (3) As the bud grows, more glycoprotein trimers are recruited into the virion. (4) At late stage budding, virions are unable to incorporate the final copies of the trimeric glycoprotein spikes, which results in (5) fewer glycoproteins and distortions in the glycoprotein shell (top three trimers). The newly formed immature virus then leaves the ER and traffics through the Golgi, and encounters low pH in the trans-Golgi network. (6) Maturation in the trans-Golgi network results in a large conformational rearrangement and distortions across the particle. As a result of maturation, the nucleocapsid is repositioned to be concentric with the glycoprotein shell.

The nucleocapsid core was found to be eccentrically positioned in an immature flavivirus, similar to its positioning in herpesvirus and HIV (97, 98). However, the flavivirus core is unique in that it repositions as a result of maturation. During the maturation process, the glycoproteins undergo conformational rearrangements from trimers to dimers possibly loosening capsid-glycoprotein interactions and leading to the release and centering of the nucleocapsid core. The connections between glycoprotein transmembrane domains and the core in immature ZIKV suggested that the core had icosahedral symmetry (32). Based on the asymmetric reconstructions of KUNV and ZIKV, there is at minimum, partial icosahedral symmetry in the core, at the capsid-glycoprotein contact sites. Partial icosahedral symmetry in nucleocapsid cores is not limited to flaviviruses. The cores of alphaviruses and hepatitis B virus were assumed to be icosahedral, but have been found to assemble with imperfect icosahedral symmetry (99, 100).

By avoiding the assumption of icosahedral symmetry, it has here been possible to determine the structure of an immature particle during early stages of assembly and budding. It would seem probable that other enveloped viruses might have a similar assembly process within a cell.

CHAPTER 4. PROTEOMIC PROFILING OF EXTRACELLULAR VESICLES INDUCED IN DENGUE VIRUS INFECTION

4.1 Chapter Summary

DENV modulates host cell pathways during an infection to promote its replication, assembly, and entry into new cells. Extracellular vesicles (EVs) that are released by host cells have been shown to reprogram metabolic and signaling pathways in neighboring cells, but it is unknown how they are altered by DENV infection. EVs are heterogeneous in size and cargo, and without strong biomarkers to identify EV populations, it is challenging to define their role in DENV infection. A method to purify and evaluate EVs using sucrose gradient ultracentrifugation and negative stain EM was developed. Proteomic analysis of the DENV-induced EVs compared to mock identified four DENV-enriched proteins that can be used to pull out EV populations and advance mechanistic studies of EVs.

4.2 Introduction

Extracellular vesicles (EVs) are small, lipid-enclosed transport vesicles that carry proteins, lipids, and nucleic acids from one cell to another (101). Heterogeneous in size and content, they are utilized by cells for communication, for example to influence metabolic pathways in neighboring cells. Due to the small size (~100 nm in diameter) and complexity of EVs, it remains a challenge to study pure EV populations (102). It is common to see several methods of purification attempted in a given study, for example a recent EV publication used both differential ultracentrifugation and an EV isolation kit for purification (103). There is also confusion about how to classify EVs, as no consistent biomarkers have emerged from proteomics analyses (104).

Understanding the role of EVs in viral infection is significant because EVs contribute to viral transmission and pathogenesis, as well as to the host immune response. In general, EVs have been shown to promote both the immune response and viral infection. For hepatitis C virus (HCV), a member of the *Flaviviridae* family, it was determined that EVs from HCV-infected Huh-7.5 cells transported HCV RNA to non-permissive dendritic cells and activated their interferon response (105). Alternatively, EVs isolated from HCV-infected Huh-7.5 cells and from patient sera were packaged with viral RNA that was shown to mediate transmission of HCV in hepatocytes (106).

The role of EVs in flavivirus infection, in particular for DENV, has not been well studied. EVs isolated from patient sera stained positive for E and NS1 by flow cytometry, indicating that EVs may carry DENV proteins on their surface (107). It was also shown that DENV-infected Huh-7 cells released EVs that carried infectious DENV RNA, as well as E, prM, and NS1 (108). Furthermore, DENV-infected insect cells released infectious EVs that contained viral RNA and E (109). A potential caveat of these studies is if virions and other particulates were inadvertently co-purified with EVs.

As there are no good biomarkers for EVs, we aimed here to use proteomics to identify suitable protein candidates that could be used to isolate EVs that were relevant to DENV infection. These EVs can then be used for mechanistic studies to identify their role in DENV transmission.

4.3 Materials and Methods

4.3.1 Cell culture

HEK 293T, Vero, and Huh-7 cells were grown in DMEM supplemented with 1X non-essential amino acids (NEAA) and 10% FBS at 37°C.

4.3.2 Purification of EVs by differential ultracentrifugation

The Thailand/16681/1984 strain of DENV-2 or mock virus was added to ~3 x 10^5 Huh-7 cells in a T150 at an MOI of 8. The virus was incubated with the cells in 5 mL of PBS with 1 mM $MgCl_2$, 1 mM $CaCl_2$, and 1% FBS, and rocked at room temperature for 45 minutes, and then incubated at 37°C for 15 minutes. 15 mL of DMEM with 2% FBS and 1X glutamine was added to each T150, and the cells were incubated at 37°C. At 48 hpi, CPE was observed and the media were removed and clarified at 300 x g for 15 minutes.

The 20 mL of media were spun at 32,000 RPM for 2 hours in a Ti50.2 rotor (Beckman Coulter, Inc). The supernatant was poured out, and any remaining supernatant was aspirated. Faint pellets were observed for DENV and mock, and the pellets were resuspended in 250 μL PBS.

4.3.3 Purification of EVs by OptiPrep gradient ultracentrifugation

HEK 293T cells were split into twenty 150 mm dishes. After two days of growth the media were harvested from approximately 6.5 x 10^7 cells, and clarified at 9,500 RPM for 15 minutes in a JA-10 rotor (Beckman Coulter, Inc). 400 mL of 2X PEG solution (16% PEG 8,000 and 1M NaCl) was added to the media and stirred to dissolve. The mix was incubated overnight at 4°C.

The PEG-media solution was spun at 10,000 x g in a JA-10 rotor (Beckman Coulter, Inc) for 50 minutes. There was a very large pellet present on the sides of the bottle. The pellet was resuspended in 20 mL of HEPES buffer (12 mM HEPES pH 8, 120 mM NaCl, 2 mM $MgCl_2$) and spun in a Ti50.2 rotor (Beckman Coulter, Inc) at 32,000 RPM for 2 hours. The pellet was yellow and brown colored, and was resuspended in 1 mL of HEPES buffer.

A discontinuous OptiPrep gradient was made with 10-20-25-30-40% OptiPrep in HEPES buffer. 1.5 mL of each layer was underlaid to make the gradient, with 2 mL of the 10% layer. The resuspended pellets were spun at 3,000 x g for 1 minute to pellet any aggregates. The supernatant

was removed and layered on top of the gradient. The aggregated pellet was then washed with 0.5 mL of HEPES buffer and spun again, with the supernatant added to the top of the gradient. The gradient was spun at 32,000 RPM in a SW41 rotor (Beckman Coulter, Inc) for 2 hours. Bands were visible at the 10/20% and 20/25% interface. ~1 mL fractions were collected using a peristaltic pump from the bottom of the tube.

4.3.4 SDS-PAGE and western blot

4 μL of sample was added to 1 μL of 5X reducing dye and boiled for 5 minutes. The sample was loaded onto a 12% polyacrylamide gel and run at 170 V for 1 hour. The gel was boiled in Coomassie Brilliant Blue R-250 for ~10 seconds, and then rocked at room temperature for 5 minutes before destaining.

The SDS-PAGE for western blots was run similarly, except with 16 μL of sample added to 4 μL of 5X reducing dye. After electrophoresis, the gel was transferred onto a nitrocellulose membrane at 100 V for 1 hour. Then the membrane was blocked in 2.5% milk in PBS-T overnight at 4°C. The next day, the membrane was quickly washed with PBS-T, and then incubated with 10 mL of mouse anti-CD81 (JS-81, BD Biosciences) at a dilution of 1:500 in PBS-T for 1 hour. The membrane was washed three times for 5 minutes each in PBS-T, and then incubated with 10 mL of the secondary antibody (IR Dye 800CW Goat anti-Mouse, LI-COR Biosciences) at a dilution of 1:10,000 in PBS-T for 1 hour in the dark. The membrane was again washed three times, and then imaged using the Odyssey CLx Imaging System (LI-COR Biosciences).

4.3.5 Agarose gel electrophoresis

8.4 μL of gradient fractions were added to 1.6 μL of 6X dye and loaded onto a 0.8% agarose gel. The gel was run at 140 V and nucleic acids were visualized with the GelDoc-It Imager (UVP).

4.3.6 Negative stain EM

Negative staining was performed following the droplet method (110). Briefly, 3 μL of sample was added to a glow-discharged copper grid. The solution was blotted away after ~15 minutes, and then the grid was washed twice with 25 μL of steamed distilled water, while blotting in-between washes. The grid was then stained with 10 μL of 0.75% uranyl formate, which was blotted away after 10 seconds. The grid was then air dried.

Transmission EM was done using the Tecnai T20 (FEI) or Tecnai T12 (FEI). The nominal magnifications used were between 40,000-50,000X, which corresponded to pixel sizes of ~6-9 Å/pixel.

4.3.7 Purification of EVs by sucrose gradient ultracentrifugation

HEK293T cells and Veros were split into twenty 150 mm dishes, and the media were harvested after 3 days of growth. The media were clarified at 5,000 RPM for 30 minutes in a JA-10 rotor (Beckman Coulter, Inc). 100 mL of 5X PEG solution (40% PEG 8,000 2.5 M NaCl) was added and inverted to dissolve. The mix was incubated at 4°C for 3 hours. The PEG solution was spun at 15,000 x g in a JA-10 rotor (Beckman Coulter, Inc) for 50 minutes. There was a large white pellet for both 293T and Vero media. The pellets were resuspended in 20 mL of TNE (12 mM Tris pH 8, 120 mM NaCl, 1 mM EDTA), and spun in a Ti50.2 rotor (Beckman Coulter, Inc) at 10,000 x g overnight.

The pellets were resuspended in 1 mL of TNE and added to 1 mL of 85% sucrose in an Ultra-Clear tube (Beckman Coulter, Inc). 5 mL of 35% sucrose was overlaid, followed by 3 mL of 5% sucrose on top, based on a flotation assay protocol (111). The gradient was spun in a SW41 rotor (Beckman Coulter, Inc) at 38,000 RPM for 2 hours. The gray band present at the 5/35% interface was extracted with a 22G needle and syringe and buffer exchanged four times into TNE.

Purification of DENV- and mock-infected Huh-7 media was performed similarly, with the following modifications. Three replicates of DENV-2 and mock virus were performed with ten 150 mm dishes of ~1 x 10^8 total Huh-7 cells. One replicate for DENV and mock was performed earlier and with a different DENV stock. The MOI for the infections was ~0.5. The virus was added to the cells in 5 mL of DMEM in 2% FBS, and the cells were rocked at room temperature for 1 hour. 15 mL of DMEM and 2% FBS was then added, and cells were incubated at 37°C. The media were harvested when CPE was observed, which occurred at 48 hpi for one replicate and 68 hpi for the other two replicates. After PEG precipitation, the resuspended PEG pellets were spun in a Ti50.2 rotor (Beckman Coulter, Inc) at 32,000 RPM for 2 hours. The rest of the purification was performed as described for HEK 293T and Veros. Following purification, the samples were heat-inactivated at 55°C for 30 minutes before submitting to the Bindley Bioscience Center mass spectrometry facility.

4.3.8 Protein extraction and digestion

Samples were dried for 1 hour in a vacuum centrifuge and 100 μL of ammonium bicarbonate (ABC) was added to the pellets. Samples were then homogenized in a barocycler (Pressure Biosciences) set to 35 kpsi for 20 seconds, followed by atmospheric pressure for 10 seconds, for 90 cycles. The samples were compared to BSA standards using a bicinchoninic acid (BCA) assay to estimate protein concentration. The sample was then precipitated with four volumes of acetone, and stored at -20°C overnight.

Acetone precipitated samples were spun at 14,000 RPM for 15 minutes. The supernatant was removed and resuspended in acetone. The samples were incubated at -20°C for 15 minutes, then spun at 14,000 RPM for 10 minutes. The supernatant was removed and the sample was dried in a vacuum centrifuge for 15 minutes. 10 μL of 10 mM DTT/urea was added and the samples

were placed in a rotary shaker for 30 minutes at 37°C. Next, 10 µL of the alkylating solution was added (195 µL acetonitrile (ACN), 4 µL 2-iodoethanol, 1 µL triethylphosphine) and again samples were placed in a rotary shaker for 30 minutes at 37°C. Following the reduction and alkylation steps, samples were dried in vacuum centrifuge for 30 minutes.

20 µg of trypsin-LysC was dissolved in 400 µL 25 mM ABC and 80 µL was added to the samples for digestion. Digestion occurred at 50°C in a barocycler (Pressure Biosciences) set to 20 kpsi for 50 seconds, then atmospheric pressure for 10 seconds, for 60 cycles. Peptides were then purified with a C18 MicroSpin columns (Nest Group) following manufacturer's instructions. Peptides were eluted with 80% ACN, 0.1% formic acid and dried in a vacuum centrifuge for 1 hour. The samples were stored at -20°C prior to LC-MS/MS.

4.3.9 LC-MS/MS

This paragraph was provided by Victoria Hedrick at the Bindley Bioscience Center.

Digested samples were analyzed using the Dionex UltiMate 3000 RSLC Nano System which was coupled to a Q Exactive™ HF Hybrid Quadrupole-Orbitrap Mass Spectrometer (Thermo Scientific, Waltham, MA). Peptides were first loaded onto a 300 µm i.d. x 5mm C18 PepMap™ 100 trap column and washed with 98% purified water/2% acetonitrile (ACN)/0.01% formic acid (FA) using a flow rate of 5 µl/minute. After 5 minutes, the trap column was switched in-line with a 75 µm x 50 cm reverse phase Acclaim™ PepMap™ RSLC C18 analytical column heated to 50°C. Peptides were separated over the analytical column using a 120 minute method at a flow rate of 300 nl/minute. Mobile phase A contained 0.01% FA in purified water while mobile phase B consisted of 0.01 % FA/80% ACN in purified water. The linear gradient began at 2% B and reached 10% B in 5 minutes, 30% B in 80 minutes, 45% B in 91 minutes, and 100% B in 93 minutes. The column was held at 100% B for the next 5 minutes before returning to 5% B where

it was equilibrated for 20 minutes. Samples were injected into the QE HF through the Nanospray Flex™ Ion Source fitted with an emitter tip from New Objective. MS spectra were collected from 400 to 1600 m/z at 120,000 resolution, a maximum injection time of 100 ms, and a dynamic exclusion of 15 s. The top 20 precursors were fragmented using higher-energy C-trap dissociation (HCD) at a normalized collision energy of 27%. MS/MS spectra were acquired in the Orbitrap at a resolution of 15,000 with a maximum injection time of 20ms.

4.3.10 Data analysis

Peptides were matched to proteins using MaxQuant 1.6.3.3 (112) and searched in the UniProt *H. sapiens* database (113) downloaded on February 7, 2019 combined with the DENV-2 strain 16681 protein sequences, a list of contaminants, and a reverse decoy database. Digestion was set to Trypsin and Lys-C, and chosen modifications were oxidation (M), acetyl (N-terminal) with fixed modifications iodioethanol (C). Peptide tolerance was set to 10 ppm, and label free quantification was performed. All other default options were used, including a false discovery rate of 1%.

Filtering of the dataset was performed in Excel (Microsoft). First, contaminants and reverse hits were removed, as well as proteins with zero raw intensity values and any proteins with zero or one MS/MS counts. This led to a list of 1,554 proteins. The list was further filtered to 226 proteins by keeping only proteins that were observed in ≥ 2 replicates in either the DENV or mock datasets. Of the 226 proteins, 141 were found in only the DENV sample, one was only found in the mock sample, and 84 were found in both datasets. To avoid data value imputation, the list was further filtered to keep only proteins that appeared in all three replicates. This list included four proteins found only in the DENV sample, and 32 proteins found in both DENV and mock. The label free quantification (LFQ) values were then $\log_2$-transformed and averages for the replicates

were calculated. Fold enrichment was calculated by subtracting the transformed mock averages from the DENV transformed averages. A two-tailed Student's t-test was used to calculate statistical significance. A protein was considered statistically significant if it had a p-value of 0.05 or greater, and a fold enrichment of three or greater. Only four proteins fit this criteria.

4.3.11 Gene Ontology (GO) analysis

The protein IDs of the 141 proteins that were identified in only the DENV sample were submitted to the Gene Ontology knowledgebase (114). The top five results based on p-values in biological process, molecular function and cellular component were reported.

4.4 Results

In order to use proteomics to identify potential biomarkers of DENV-induced EVs, EVs had to be separated from contaminants in the media. In the literature there is no consistent method for isolating EVs from cell media, so several strategies were attempted. Differential ultracentrifugation of mock-infected Huh-7 cells yielded EVs based on the characteristic donut shape seen in negative stain EM (Figure 4.1). However, the high protein contamination observed by negative stain limited the usability of the purification for proteomics analysis, and therefore EV purification by gradient ultracentrifugation was performed.

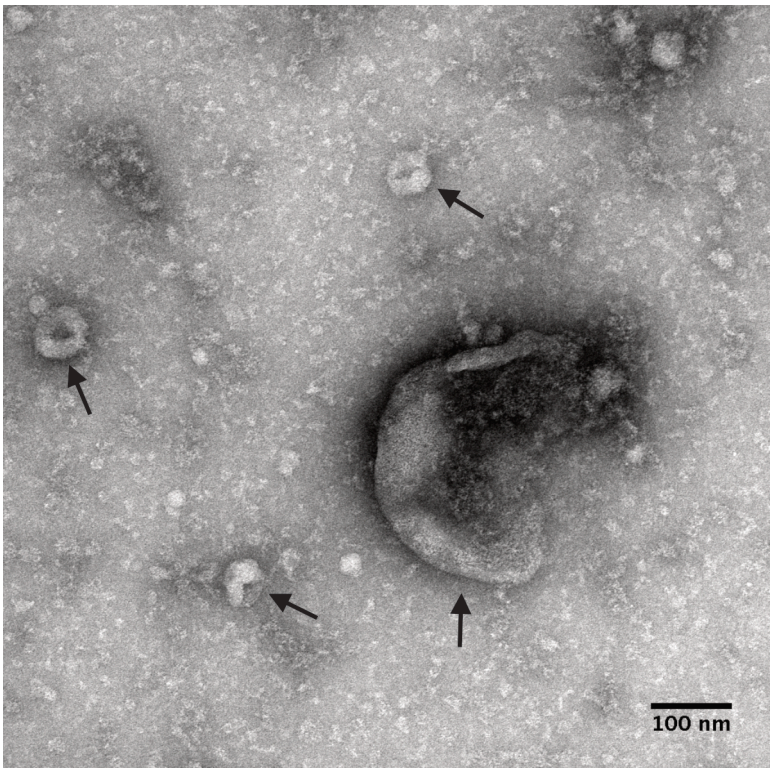

Figure 4.1 Mock-infected Huh-7 EVs isolated by differential ultracentrifugation

Negative stain EM of purified Huh-7 media with EVs (black arrows). There is high protein contamination seen in the background. Pixel size: 9.24 Å/pixel.

As it was unclear which gradient reagent would work best in terms of both separation and EV stability, OptiPrep was initially used based on its extensive use in the literature for EV separation. Additionally, CD81, a tetraspanin protein and proposed biomarker of EVs, was used to identify EVs within the gradient. In a pilot study, mock-infected HEK 293T media were purified with an OptiPrep gradient and fractionated (Figure 4.2A). A CD81 western blot of the gradient-fractionated media indicated that CD81 was found in primarily fractions 5-8 (Figure 4.2B). The fractions were also run on an agarose gel to identify fractions containing nucleic acids, as EVs are known to be packaged with RNAs. Fractions 5-7 showed bands for nucleic acids, in agreement with CD81 (Figure 4.2C). When these fractions were combined, concentrated and run on an SDS-PAGE gel, there was a high number of protein bands present (Figure 4.2D).

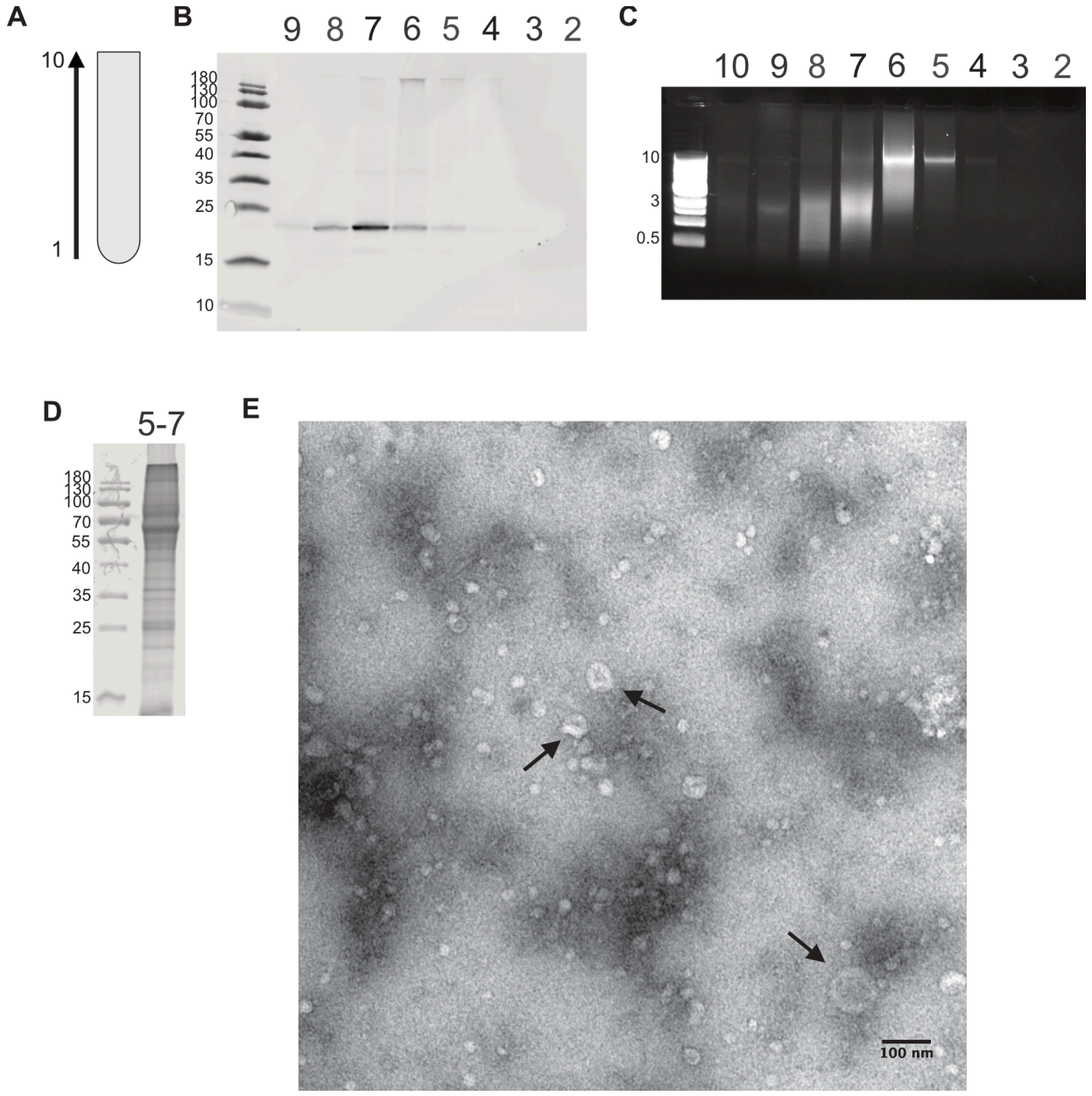

Figure 4.2 Characterization of HEK 293T EV purification

OptiPrep gradient-fractionated EV prep. (**A**) Fractions were collected from bottom to top (1 is bottom, 10 is top). (**B**) CD81 western blot of fractions. The CD81 band is seen at ~25 kDa, with fraction 7 containing the strongest band. (**C**) Agarose gel of fractions, with nucleic acid seen most brightly in fraction 6 and 7. (**D**) SDS-PAGE of pooled and concentrated fractions 5-7. (**E**) Negative stain EM of pooled and concentrated fractions 5-7 with observed EVs (black arrows). Pixel size: 6.66 Å/pixel.

Negative stain EM was used to evaluate the purity and concentration of EVs in the combined fractions, which showed that although EVs were recovered, there was high protein contamination (Figure 4.2E). The contamination and low number of EVs recovered indicated that OptiPrep was not an ideal gradient solution for separation. Sucrose gradients are frequently used for subcellular fractionation as well as liposome flotation assays. Therefore, it was hypothesized that sucrose solution might better separate EVs from proteins with similar density properties. Additionally, in the flotation assay, liposomes are added to the bottom of the gradient and floated up. This method has been shown to reduce aggregated protein co-purifying with liposomes, and was therefore used to separate EVs.

EVs were isolated from mock-infected HEK 293T and Vero media with sucrose gradients, following a similar procedure as a flotation assay (111). The purified samples were negative stained and imaged. Negative stain EM showed that the EVs from both cell types were free of background protein (Figure 4.3).

Therefore, the adapted flotation assay protocol was used to purify EVs from mock and DENV-infected Huh-7 cells. Negative stain EM showed that the EVs were relatively clean from protein and particulate contamination (Figure 4.4). The EVs were heterogenous and ranged in size from ~40 to 300 nm in diameter.

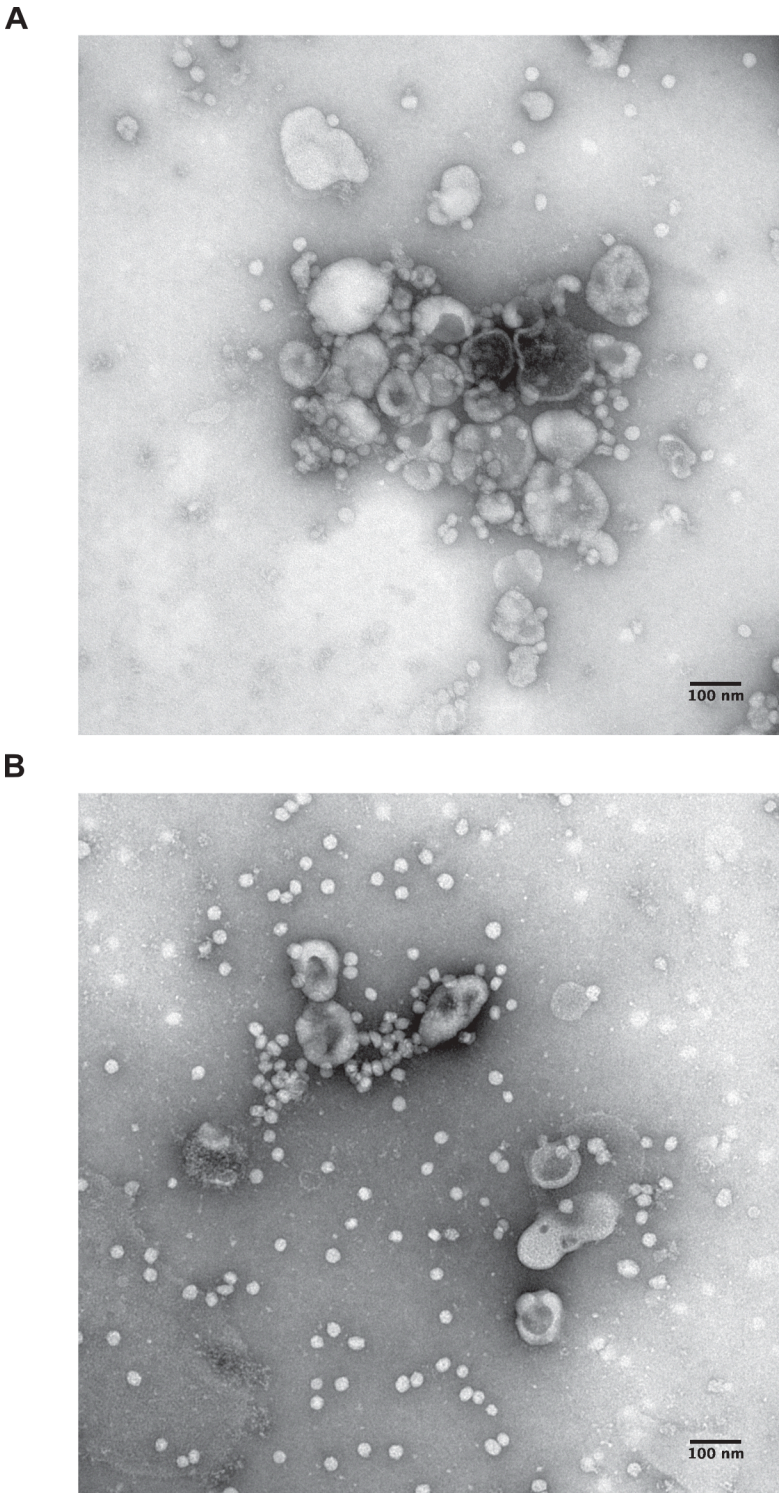

Figure 4.3 EVs isolated from mock-infected 293Ts and Veros

Negative stain EM of EVs purified using a sucrose gradient. EVs were purified from (**A**) HEK 293T media and (**B**) Vero media. Pixel size: 6.66 Å/pixel.

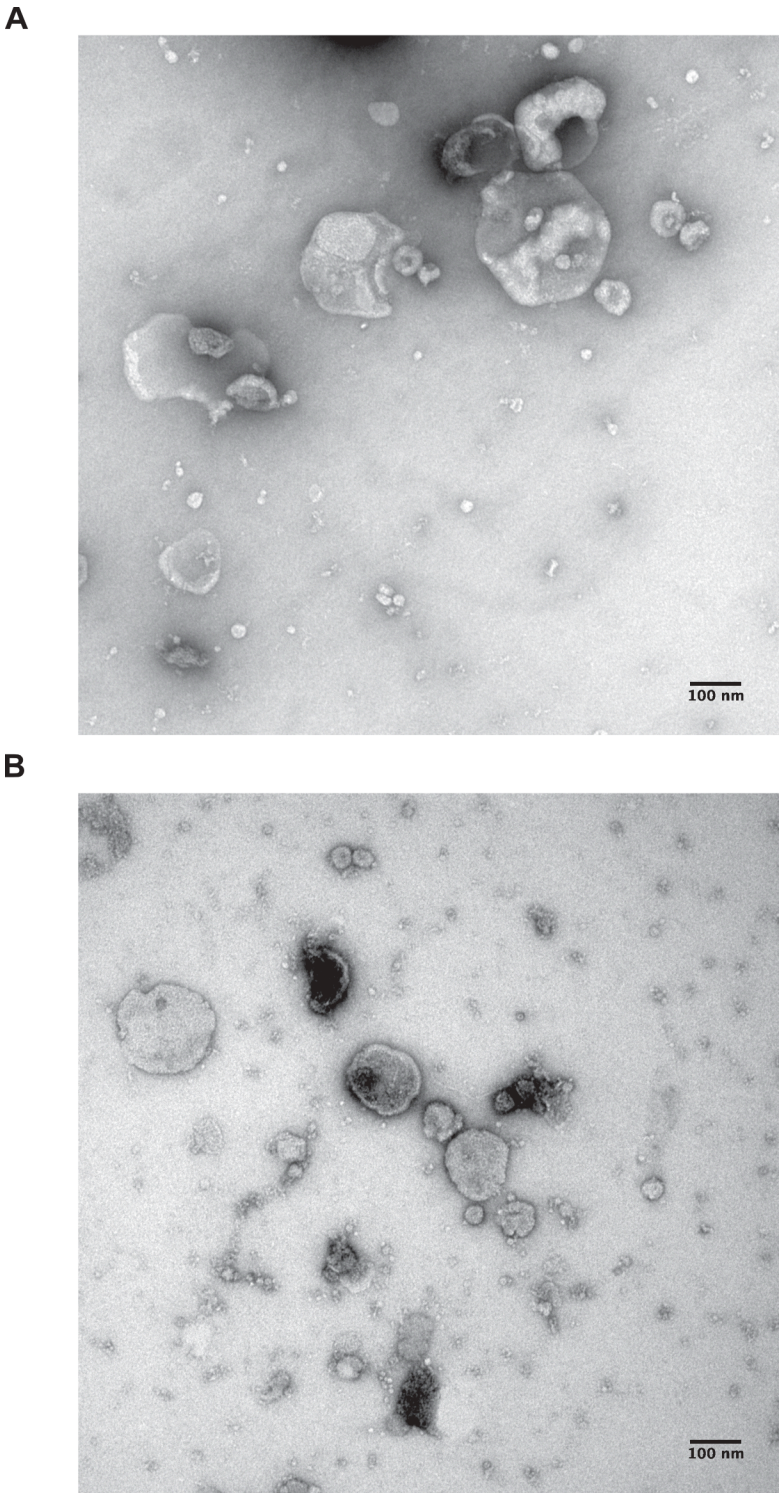

Figure 4.4 EVs isolated from infected Huh-7's

Negative stain EM of Huh-7 EVs purified by sucrose gradient ultracentrifugation. (**A**) Mock-infected Huh-7 EVs. (**B**) DENV-infected Huh-7 EVs. Pixel size: 6.66 Å/pixel.

Three replicates of EV samples for mock and DENV were prepared for mass spectrometry and analyzed by LC-MS/MS. Database searching and label-free quantification (LFQ) was performed with Maxquant 1.6.3.3 (112) which identified 1,554 proteins. LFQ values represent normalized peptide ion intensities. DENV proteins that were found in the protein list in ≥ 2 replicates were the structural proteins E, M, and C as well as nonstructural protein 1 (NS1) (Table 4.1).

Table 4.1 DENV proteins identified in EV sample

Label free quantification (LFQ) values for DENV proteins identified in ≥ 2 replicates were log_2-transformed and averaged.

Protein	Average Log_2 LFQ intensity
Structural proteins	
E	31.2
M	27.3
C	27.7
Non structural proteins	
NS1	29.3

Based on the average LFQ values, there was higher E and NS1 in the sample, and similar amounts of M and C. A western blot for DENV E confirmed that E was present in all DENV samples (Figure 4.5).

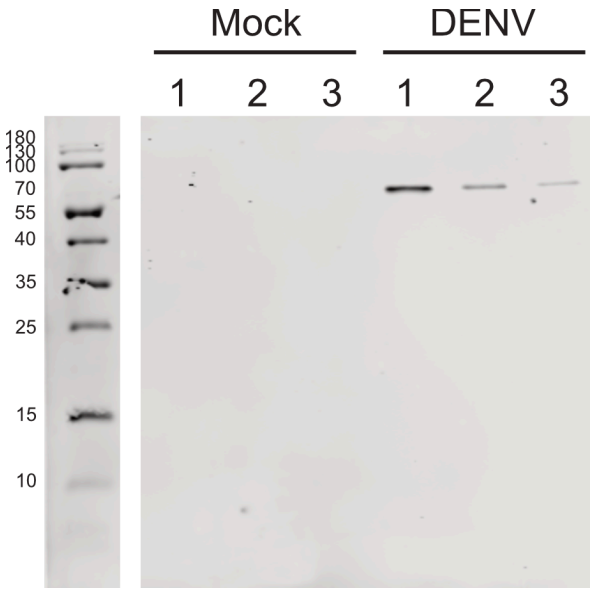

Figure 4.5 Western blot for DENV E

Three replicates for mock-infected and DENV-infected Huh-7 were probed with 4G2 mAb. E: ~54 kDa.

The dataset was initially filtered to identify proteins found in ≥ 2 replicates of the DENV sample and not the mock sample (DENV-enriched). Proteins that were in ≥ 2 replicates of the mock sample and not the DENV sample (DENV-depleted) were also searched for, but only one protein, a keratin, was identified, which is a common contaminant for mass spectrometry. The list of DENV-enriched proteins included 141 proteins. The proteins were analyzed by gene ontology (GO) analysis, which indicated that the DENV-enriched proteins were generally involved in vesicular transport and were components of extracellular vesicles, confirming that the purification procedure successfully isolated EVs (Table 4.2).

Table 4.2 GO term analysis of EV proteins found in DENV and not mock sample

Proteins identified in ≥ 2 replicates in the DENV sample and not the mock sample (DENV-enriched) were searched in the GO database for biological processes, molecular functions and cellular components. The top five results for each category are shown. Count in gene set indicates the number of proteins that were found in the dataset compared to the GO reference list. P-value refers to a statistical over-representation of input genes relative to the reference list.

GO Term	Count in Gene Set	P-value
Biological Process		
Localization	95 of 5651	2.03×10^{-19}
Transport	84 of 4467	9.55×10^{-19}
Establishment of localization	85 of 4588	1.11×10^{-18}
Exocytosis	37 of 781	6.45×10^{-17}
Regulated exocytosis	35 of 693	1.26×10^{-16}
Molecular Function		
Cell adhesion molecule binding	33 of 483	9.01×10^{-20}
Cadherin binding	23 of 315	1.83×10^{-13}
Protein binding	121 of 11890	3.99×10^{-10}
Protein-containing complex binding	33 of 1096	1.14×10^{-9}
Binding	135 of 15185	2.32×10^{-9}
Cellular Component		
Extracellular exosome	114 of 2096	6.59×10^{-83}
Extracellular vesicle	114 of 2117	1.93×10^{-82}
Extracellular organelle	114 of 2119	2.14×10^{-82}
Vesicle	122 of 3812	9.07×10^{-66}
Extracellular region part	117 of 3529	1.47×10^{-62}

To identify potential EV biomarkers of DENV infection, the list of proteins was more stringently filtered to only the proteins found in all three replicates, which reduced the dataset to 36 proteins. Label free quantification was used to calculate the enrichment of each protein along with statistical significance. Hits were classified as those with greater than threefold enrichment and p-values of 0.05 or greater. Based on the criteria, only four proteins remained as candidates, cystatin-A (CSTA), filamin B (FLNB), fibrinogen beta chain (FGB), and endothelin converting enzyme 1 (ECE1) (Figure 4.6).

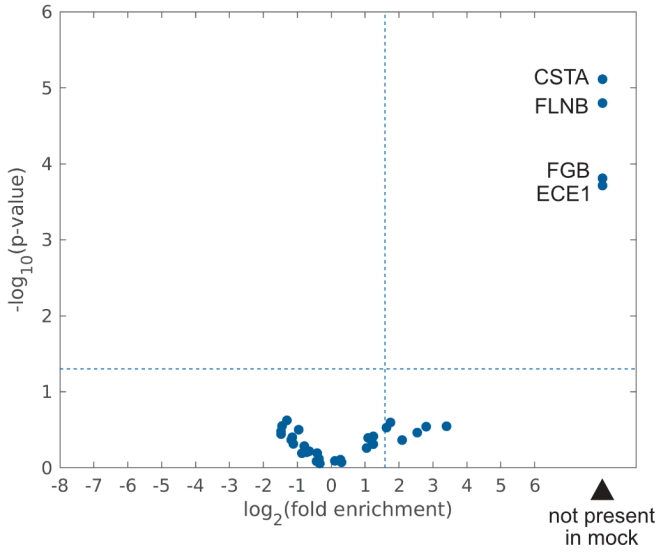

Figure 4.6 DENV-enriched Huh-7 EV proteins

Volcano plot of DENV-enriched host proteins relative to mock. The horizontal line designates a p-value of 0.05, and the vertical line designates threefold enrichment, which was the criteria used to identify candidate proteins. Four proteins that were only found in the DENV sample were identified within these thresholds.

The properties of these four proteins was investigated in the literature (Table 4.3). CSTA is a member of the cystatin family which are known inhibitors of cysteine proteases, such as cathepsins found in lysosomes (115). FLNB cross-links actin and is an important component of the cytoskeleton and the extracellular matrix. FGB is involved in forming fibrin for blood clotting. Lastly, ECE1 is a glycosylated metalloprotease that cleaves and activates endothelin, a potent vasoconstrictor (116). It has also been found to degrade proteins and peptides including α-synuclein, bradykinin, and somatostatin (117). As an integral membrane protein it resides on the plasma membrane and in intracellular and extracellular vesicles (118, 119).

Table 4.3 Properties of DENV-enriched Huh-7 protein hits

Protein	Protein ID	Type	Mol. Weight (kDa)
Cystatin-A	CSTA	Soluble	11
Filamin B	FLNB	Soluble	278
Fibrinogen beta chain	FGB	Soluble	56
Endothelin converting enzyme 1	ECE1	Integral membrane protein	87

CSTA, FLNB, and FGB are soluble proteins, and are therefore either EV cargo or peripherally associated with EV lipids or membrane proteins. In contrast, ECE1 is an integral membrane protein and likely found inside the EV membrane. These proteins provide potential biomarkers for DENV infection, as well as immunoprecipitation targets for pulling down EV subpopulations, and can guide investigation into the role of EVs in DENV infection.

4.5 Discussion

As methods for EV purification are not standardized, method development of the purification procedure was necessary in order to obtain EV proteomics datasets. Optimization required being able to identify when EVs were isolated free of impurities. Although various biochemical methods were attempted, including western blots, ultimately negative stain EM was the best method for confirming that EVs were pure. Compared to virus purifications, such as those described in Chapter 3, the yields of EVs from twenty dishes of cell media was low. It is possible that the purification procedure destroyed EVs, or that cell lines released fewer EVs than expected. HEK 293Ts, Veros, and Huh-7's were all found to release EVs in amounts that were observable by negative stain EM. Negative stain EM unfortunately dehydrates EVs and changes their shape, so it was difficult to analyze the structural heterogeneity in EVs. Improvements in the purification scheme should yield sufficient quantities of EVs for cryo-EM, which would allow for a full characterization of EV structure.

The DENV proteins NS1, E, M and C were all identified by mass spectrometry in the EV sample. It is likely that virions co-purified with EVs even following the flotation assay, and indeed virions were observed in EV purifications in negative stain EM. Previous studies which used ultracentrifugation to isolate flavivirus EVs also likely contained virions and other particulates (109). With the identification of EV biomarkers and use of affinity purification, it will be possible to independently evaluate whether EVs carry viral proteins or RNA because these samples will not be contaminated by virions.

Mass spectrometry of Huh-7 EVs identified 141 proteins that were enriched in the DENV sample over mock. These proteins were involved in vesicular transport and were known components of EVs. From this dataset, only four proteins were identified that were both threefold enriched and statistically significant. These were the proteins CSTA, FLNB, FGB, and ECE1. While these proteins do not interact, they have overlapping known functions, for example FGB and ECE1 are involved in vascular remodeling. However, the role of these proteins in DENV infection remains to be validated and evaluated, as well as if they are present in the same EVs or different populations. As candidate EV biomarkers for DENV infection, these proteins will facilitate future mechanistic studies.

REFERENCES

1. Campbell GL, Marfin AA, Lanciotti RS, Gubler DJ (2002) West Nile virus. *Lancet Infect Dis* 2:519–29.
2. Hall RA, Scherret JH, Mackenzie JS (2001) Kunjin virus: an Australian variant of West Nile? *Ann N Y Acad Sci* 951:153–160.
3. Gubler DJ, Vasilakis N, Musso D (2017) History and Emergence of Zika Virus. *J Infect Dis* 216:S860–S867.
4. Duffy MR, et al. (2009) Zika Virus Outbreak on Yap Island, Federated States of Micronesia. *N Engl J Med* 360:2536–2543.
5. Halstead S (1988) Pathogenesis of dengue: challenges to molecular biology. *Science* 239:476–481.
6. Gubler DJ (1998) Dengue and dengue hemorrhagic fever. *Clin Microbiol Rev* 11:480–496.
7. Bhatt S, et al. (2013) The global distribution and burden of dengue. *Nature* 496:504–507.
8. Allison SL, et al. (1995) Oligomeric rearrangement of tick-borne encephalitis virus envelope proteins induced by an acidic pH. *J Virol* 69:695–700.
9. Klein DE, Choi JL, Harrison SC (2013) Structure of a dengue virus envelope protein late-stage fusion intermediate. *J Virol* 87:2287–2293.
10. Lindenbach BD, Murray CL, Thiel H-J, Rice CM (2013) *Flaviviridae* (Wolters Kluwer/Lippincott Williams & Wilkins Health).
11. Mukhopadhyay S, Kuhn RJ, Rossmann MG (2005) A structural perspective of the flavivirus life cycle. *Nat Rev Microbiol* 3:13–22.
12. Zhang Y, et al. (2003) Structures of immature flavivirus particles. *EMBO J* 22:2604–2613.
13. Yu I-M, et al. (2008) Structure of the Immature Dengue Virus at Low pH Primes Proteolytic Maturation. *Science* 319:1834–1837.
14. Yu I-M, et al. (2009) Association of the pr peptides with dengue virus at acidic pH blocks membrane fusion. *J Virol* 83:12101–12107.
15. Sirohi D, Kuhn RJ (2017) Zika Virus Structure, Maturation, and Receptors. *J Infect Dis* 216:S935–S944.
16. Kuhn RJ, et al. (2002) Structure of dengue virus: implications for flavivirus organization, maturation, and fusion. *Cell* 108:717–725.

17. Prasad BVV, Schmid MF (2012) *Principles of Virus Structural Organization* (Springer US).
18. Caspar DL, Klug A (1962) Physical principles in the construction of regular viruses. *Cold Spring Harb Symp Quant Biol* 27:1–24.
19. Johnson JE, Speir JA (1997) Quasi-equivalent viruses: a paradigm for protein assemblies. *J Mol Biol* 269:665–675.
20. Rossmann MG, Johnson JE (1989) Icosahedral RNA Virus Structure. *Annu Rev Biochem* 58:533–569.
21. Hasan SS, et al. (2017) A human antibody against Zika virus crosslinks the E protein to prevent infection. *Nat Commun* 8:14722.
22. Sirohi D, et al. (2016) The 3.8 A resolution cryo-EM structure of Zika virus. *Science* 352:467–470.
23. Mukhopadhyay S, Kim BS, Chipman PR, Rossmann MG, Kuhn RJ (2003) Structure of West Nile Virus. *Science* 302:248–248.
24. Wang X, et al. (2017) Near-atomic structure of Japanese encephalitis virus reveals critical determinants of virulence and stability. *Nat Commun* 8:14.
25. Rey FA, Heinz FX, Mandl C, Kunz C, Harrison SC (1995) The envelope glycoprotein from tick-borne encephalitis virus at 2 Å resolution. *Nature* 375:291–298.
26. Li L, et al. (2008) The Flavivirus Precursor Membrane-Envelope Protein Complex: Structure and Maturation. *Science* 319:1830–1834.
27. Zhang W, Kaufmann B, Chipman PR, Kuhn RJ, Rossmann MG (2013) Membrane curvature in flaviviruses. *J Struct Biol* 183:86–94.
28. Zhang W, et al. (2003) Visualization of membrane protein domains by cryo-electron microscopy of dengue virus. *Nat Struct Biol* 10:907–912.
29. Zhang Y, Kostyuchenko VA, Rossmann MG (2007) Structural analysis of viral nucleocapsids by subtraction of partial projections. *J Struct Biol* 157:356–364.
30. Ma L, Jones CT, Groesch TD, Kuhn RJ, Post CB (2004) Solution structure of dengue virus capsid protein reveals another fold. *Proc Natl Acad Sci U S A* 101:3414–3419.
31. Kostyuchenko VA, Zhang Q, Tan JL, Ng T-S, Lok S-M (2013) Immature and Mature Dengue Serotype 1 Virus Structures Provide Insight into the Maturation Process. *J Virol* 87:7700–7707.

32. Prasad VM, et al. (2017) Structure of the immature Zika virus at 9 Å resolution. *Nat Struct Mol Biol* 24:184–186.
33. Zhang Y, Kaufmann B, Chipman PR, Kuhn RJ, Rossmann MG (2007) Structure of Immature West Nile Virus. *J Virol* 81:6141–6145.
34. Kuhn RJ, Dowd KA, Beth Post C, Pierson TC (2015) Shake, rattle, and roll: Impact of the dynamics of flavivirus particles on their interactions with the host. *Virology* 479–480:508–517.
35. Austin SK, et al. (2012) Structural Basis of Differential Neutralization of DENV-1 Genotypes by an Antibody that Recognizes a Cryptic Epitope. *PLoS Pathog* 8:e1002930.
36. Zhao H, et al. (2016) Structural Basis of Zika Virus-Specific Antibody Protection. *Cell* 166:1016–1027.
37. Dowd KA, Mukherjee S, Kuhn RJ, Pierson TC (2014) Combined Effects of the Structural Heterogeneity and Dynamics of Flaviviruses on Antibody Recognition. *J Virol* 88:11726–11737.
38. Lok S-M, et al. (2008) Binding of a neutralizing antibody to dengue virus alters the arrangement of surface glycoproteins. *Nat Struct Mol Biol* 15:312–317.
39. Fibriansah G, et al. (2013) Structural Changes in Dengue Virus When Exposed to a Temperature of 37 C. *J Virol* 87:7585–7592.
40. Zhang X, et al. (2013) Dengue structure differs at the temperatures of its human and mosquito hosts. *Proc Natl Acad Sci U S A* 110:6795–6799.
41. Kaufmann B, et al. (2010) Neutralization of West Nile virus by cross-linking of its surface proteins with Fab fragments of the human monoclonal antibody CR4354. *Proc Natl Acad Sci* 107:18950–18955.
42. Pierson TC, Diamond MS (2012) Degrees of maturity: the complex structure and biology of flaviviruses. *Curr Opin Virol* 2:168–175.
43. Dejnirattisai W, et al. (2015) A new class of highly potent, broadly neutralizing antibodies isolated from viremic patients infected with dengue virus. *Nat Immunol* 16:170–177.
44. Pierson TC, et al. (2007) The Stoichiometry of Antibody-Mediated Neutralization and Enhancement of West Nile Virus Infection. *Cell Host Microbe* 1(2):135–145.

45. Tsai W-Y, et al. (2018) Potent Neutralizing Human Monoclonal Antibodies Preferentially Target Mature Dengue Virus Particles: Implication for Novel Strategy for Dengue Vaccine. *J Virol* 92. doi:e00556-18.
46. Zhang Y, et al. (2003) Structures of immature flavivirus particles. *EMBO J* 22:2604–2613.
47. Zhu P, et al. (2006) Distribution and three-dimensional structure of AIDS virus envelope spikes. *Nature* 441:847–852.
48. Oliphant T, et al. (2005) Development of a humanized monoclonal antibody with therapeutic potential against West Nile virus. *Nat Med* 11:522–530.
49. Nybakken GE, et al. (2005) Structural basis of West Nile virus neutralization by a therapeutic antibody. *Nature* 437:764–769.
50. Lee PD, et al. (2013) The Fc Region of an Antibody Impacts the Neutralization of West Nile Viruses in Different Maturation States. *J Virol* 87:13729–13740.
51. Kaufmann B, et al. (2006) West Nile virus in complex with the Fab fragment of a neutralizing monoclonal antibody. *Proc Natl Acad Sci U S A* 103:12400–12404.
52. Kaufmann B, et al. (2009) Capturing a Flavivirus Pre-Fusion Intermediate. *PLoS Pathog* 5:e1000672.
53. Blundell, T.L., Johnson LN (1976) *Protein Crystallography* (Academic Press).
54. Petsko GA (1985) Preparation of isomorphous heavy-atom derivatives. *Methods Enzymol* 114:147–56.
55. Campbell ID, Dwek RA (1984) *Biological spectroscopy* (Benjamin/Cummings Pub. Co., Menlo Park, Calif.).
56. Cheng N, et al. (1999) Tetrairidium, a Four-Atom Cluster, Is Readily Visible as a Density Label in Three-Dimensional Cryo-EM Maps of Proteins at 10–25 Å Resolution. *J Struct Biol* 127:169–176.
57. Braig K, Simon M, Furuya F, Hainfeld JF, Horwich AL (1993) A polypeptide bound by the chaperonin groEL is localized within a central cavity. *Proc Natl Acad Sci U S A* 90:3978–3982.
58. Kelly DF, Taylor KA (2005) Identification of the β1-integrin binding site on α-actinin by cryoelectron microscopy. *J Struct Biol* 149:290–302.
59. Zivanov J, et al. (2018) New tools for automated high-resolution cryo-EM structure determination in RELION-3. *Elife* 7:e42166.

60. Scheres SHW (2012) RELION: Implementation of a Bayesian approach to cryo-EM structure determination. *J Struct Biol* 180:519–530.
61. Punjani A, Rubinstein JL, Fleet DJ, Brubaker MA (2017) cryoSPARC: algorithms for rapid unsupervised cryo-EM structure determination. *Nat Methods* 14:290–296.
62. Prasad VM, et al. (2017) Structure of the immature Zika virus at 9 Å resolution. *Nat Struct Mol Biol* 24:184–186.
63. Sirohi D, et al. (2016) The 3.8 A resolution cryo-EM structure of Zika virus. *Science* 352:467–470.
64. Pettersen EF, et al. (2004) UCSF Chimera--A visualization system for exploratory research and analysis. *J Comput Chem* 25:1605–1612.
65. Tang G, et al. (2007) EMAN2: an extensible image processing suite for electron microscopy. *J Struct Biol* 157:38–46.
66. Boggon TJ, Shapiro L (2000) Screening for phasing atoms in protein crystallography. *Structure* 8:R143–R149.
67. Long F, et al. (2019) Structural basis of a potent human monoclonal antibody against Zika virus targeting a quaternary epitope. *Proc Natl Acad Sci U S A* 116:1591–1596.
68. Therkelsen MD, et al. (2018) Flaviviruses have imperfect icosahedral symmetry. *Proc Natl Acad Sci U S A* 115:11608–11612.
69. Hasan SS, Sevvana M, Kuhn RJ, Rossmann MG (2018) Structural biology of Zika virus and other flaviviruses. *Nat Struct Mol Biol* 25(1):13–20.
70. Li L, et al. (2008) The Flavivirus Precursor Membrane-Envelope Protein Complex: Structure and Maturation. *Science* 319(5871):1830–1834.
71. Zhang X, et al. (2013) Cryo-EM structure of the mature dengue virus at 3.5-Å resolution. *Nat Struct Mol Biol* 20:105–110.
72. Kostyuchenko VA, et al. (2016) Structure of the thermally stable Zika virus. *Nature* 533:425–428.
73. Dokland T, et al. (2004) West Nile Virus Core Protein. *Structure* 12(7):1157–1163.
74. Shang Z, Song H, Shi Y, Qi J, Gao GF (2018) Crystal Structure of the Capsid Protein from Zika Virus. *J Mol Biol* 430:948–962.
75. Jiang W, et al. (2006) Structure of epsilon15 bacteriophage reveals genome organization and DNA packaging/injection apparatus. *Nature* 439:612–616.

76. Guo F, et al. (2013) Visualization of uncorrelated, tandem symmetry mismatches in the internal genome packaging apparatus of bacteriophage T7. *Proc Natl Acad Sci USA* 110:6811–6816.
77. Gorzelnik K V, et al. (2016) Asymmetric cryo-EM structure of the canonical Allolevivirus Qβ reveals a single maturation protein and the genomic ssRNA in situ. *Proc Natl Acad Sci U S A* 113:11519–11524.
78. Koning RI, et al. (2016) Asymmetric cryo-EM reconstruction of phage MS2 reveals genome structure in situ. *Nat Commun* 7:12524.
79. Dai X, et al. (2017) In situ structures of the genome and genome-delivery apparatus in a single-stranded RNA virus. *Nature* 541:112–116.
80. Liu H, Cheng L (2015) Cryo-EM shows the polymerase structures and a nonspooled genome within a dsRNA virus. *Science* 349:1347–50.
81. Zhang X, et al. (2015) In situ structures of the segmented genome and RNA polymerase complex inside a dsRNA virus. *Nature* 527:531–534.
82. Lee H, et al. (2016) The novel asymmetric entry intermediate of a picornavirus captured with nanodiscs. *Sci Adv* 2:e1501929.
83. Yan R, Li K, Jiang W (2017) Real-time detection and single-pass minimization of TEM objective lens astigmatism. *J Struct Biol* 197:210–219.
84. Lander GC, et al. (2009) Appion: An integrated, database-driven pipeline to facilitate EM image processing. *J Struct Biol* 166:95–102.
85. Suloway C, et al. (2005) Automated molecular microscopy: The new Leginon system. *J Struct Biol* 151:41–60.
86. Zheng SQ, et al. (2017) MotionCor2: anisotropic correction of beam-induced motion for improved cryo-electron microscopy. *Nat Methods* 14:331–332.
87. Rohou A, Grigorieff N (2015) CTFFIND4: Fast and accurate defocus estimation from electron micrographs. *J Struct Biol* 192:216–221.
88. Roseman AM (2004) FindEM--a fast, efficient program for automatic selection of particles from electron micrographs. *J Struct Biol* 145:91–99.
89. Kucukelbir A, Sigworth FJ, Tagare HD (2014) Quantifying the local resolution of cryo-EM density maps. *Nat Methods* 11:63–65.

90. Guo F, Jiang W (2014) Single Particle Cryo-electron Microscopy and 3-D Reconstruction of Viruses. *Methods Mol Biol 1117*, pp 401–443.
91. Mastronarde DN, Held SR (2017) Automated tilt series alignment and tomographic reconstruction in IMOD. *J Struct Biol* 197:102–113.
92. Crick F, Watson J (1956) Structure of small viruses. *Nature* 177:473–475.
93. Ferlenghi I, et al. (2001) Molecular organization of a recombinant subviral particle from tick-borne encephalitis virus. *Mol Cell* 7:593–602.
94. Allison SL, et al. (2003) Two distinct size classes of immature and mature subviral particles from tick-borne encephalitis virus. *J Virol* 77:11357–66.
95. Lázaro GR, Mukhopadhyay S, Hagan MF (2018) Why Enveloped Viruses Need Cores—The Contribution of a Nucleocapsid Core to Viral Budding. *Biophys J* 114:619–630.
96. Tabata K, et al. (2016) Unique Requirement for ESCRT Factors in Flavivirus Particle Formation on the Endoplasmic Reticulum. *Cell Rep* 16:2339–2347.
97. Grünewald K, et al. (2003) Three-Dimensional Structure of Herpes Simplex Virus from Cryo-Electron Tomography. *Science* 302:1396–1398.
98. Forster F, Medalia O, Zauberman N, Baumeister W, Fass D (2005) Retrovirus envelope protein complex structure in situ studied by cryo-electron tomography. *Proc Natl Acad Sci U S A* 102:4729–4734.
99. Wang JC-Y, Chen C, Rayaprolu V, Mukhopadhyay S, Zlotnick A (2015) Self-Assembly of an Alphavirus Core-like Particle Is Distinguished by Strong Intersubunit Association Energy and Structural Defects. *ACS Nano* 9:8898–8906.
100. Pierson EE, et al. (2014) Detection of Late Intermediates in Virus Capsid Assembly by Charge Detection Mass Spectrometry. *J Am Chem Soc* 136:3536–3541.
101. Cocucci E, Meldolesi J (2015) Ectosomes and exosomes: shedding the confusion between extracellular vesicles. *Trends Cell Biol* 25:364–372.
102. Kreimer S, et al. (2015) Mass-Spectrometry-Based Molecular Characterization of Extracellular Vesicles: Lipidomics and Proteomics. *J Proteome Res* 14:2367–2384.
103. Chen G, et al. (2018) Exosomal PD-L1 contributes to immunosuppression and is associated with anti-PD-1 response. *Nature* 560:382–386.

104. Kowal J, et al. (2016) Proteomic comparison defines novel markers to characterize heterogeneous populations of extracellular vesicle subtypes. *Proc Natl Acad Sci* 113:E968–E977.
105. Dreux M, et al. (2012) Short-Range Exosomal Transfer of Viral RNA from Infected Cells to Plasmacytoid Dendritic Cells Triggers Innate Immunity. *Cell Host Microbe* 12:558–570.
106. Bukong TN, Momen-Heravi F, Kodys K, Bala S, Szabo G (2014) Exosomes from Hepatitis C Infected Patients Transmit HCV Infection and Contain Replication Competent Viral RNA in Complex with Ago2-miR122-HSP90. *PLoS Pathog* 10:e1004424.
107. Punyadee N, et al. (2015) Microparticles Provide a Novel Biomarker To Predict Severe Clinical Outcomes of Dengue Virus Infection. *J Virol* 89:1587–1607.
108. Wu Y-W, et al. (2016) Autophagy-associated dengue vesicles promote viral transmission avoiding antibody neutralization. *Sci Rep* 6:32243.
109. Vora A, et al. (2018) Arthropod EVs mediate dengue virus transmission through interaction with a tetraspanin domain containing glycoprotein Tsp29Fb. *Proc Natl Acad Sci* 115:E6604–E6613.
110. Booth DS, Avila-Sakar A, Cheng Y (2011) Visualizing Proteins and Macromolecular Complexes by Negative Stain EM: from Grid Preparation to Image Acquisition. *J Vis Exp* (58):3227.
111. Noisakran S, et al. (2008) Association of dengue virus NS1 protein with lipid rafts. *J Gen Virol* 89:2492–2500.
112. Tyanova S, Temu T, Cox J (2016) The MaxQuant computational platform for mass spectrometry-based shotgun proteomics. *Nat Protoc* 11:2301–2319.
113. Uniprot Consortium (2019) UniProt: a worldwide hub of protein knowledge. *Nucleic Acids Res* 47:D506–D515.
114. Ashburner M, et al. (2000) Gene Ontology: tool for the unification of biology. *Nat Genet* 25:25–29.
115. Turk V, Bode W (1991) The cystatins: protein inhibitors of cysteine proteinases. *FEBS Lett* 285:213–219.
116. Turner AJ, Tanzawa K (1997) Mammalian membrane metallopeptidases: NEP, ECE, KELL, and PEX. *FASEB J* 11:355–364.

117. Miners JS, Love S (2017) Endothelin-converting enzymes degrade α-synuclein and are reduced in dementia with Lewy bodies. *J Neurochem* 141:275–286.
118. Pacheco-Quinto J, Eckman EA (2013) Endothelin-converting enzymes degrade intracellular β-amyloid produced within the endosomal/lysosomal pathway and autophagosomes. *J Biol Chem* 288:5606–5615.
119. Kuruppu S, Rajapakse NW, Dunstan RA, Smith AI (2014) Nitric oxide inhibits the production of soluble endothelin converting enzyme-1. *Mol Cell Biochem* 396:49–54.

VITA

Matthew grew up in Andover, MA and attended Andover High School where he first became interested in biology. He majored in biochemistry/molecular biology at Hamilton College, and minored in mathematics. During his sophomore year at Hamilton he was accepted as a summer REU student to intern at the École Nationale Supérieure de Chimie de Paris, where he synthesized organic ligands for ring-opening polymerization initiation in the lab of Dr. Christophe Thomas under the direction of Franck Le Bideau. When he returned to Hamilton, he conducted research in the lab of Dr. Wei-Jen Chang on the fish parasite *Ichthyophthirius multifiliis*, identifying single nucleotide polymorphisms that could be used to classify parasite strains.

After graduating from Hamilton, Matthew returned to the Boston area where he worked as a research technician in Dr. Stephen Harrison's lab with Dr. Aaron Schmidt. In Steve's lab he studied influenza virus and was introduced to structural biology. He was helped determine structures of antibody Fabs in complex with influenza virus hemagglutinin that were used to inform vaccine design. As he learned crystallography he became increasingly interested in cryo-electron microscopy, a technique in structural biology that was just starting to gain prominence.

In 2014, Matthew started graduate school at Purdue University and joined Dr. Richard Kuhn's lab. There he studied flavivirus structure and maturation using cryo-electron microscopy and cryo-electron tomography. As part of his research in Richard's lab he discovered that flaviviruses have structural asymmetry, and this work was published in *PNAS*. He also investigated the role of extracellular vesicles in dengue virus infection using proteomics.

PUBLICATIONS

Therkelsen MD, Klose T, Vago F, Jiang W, Rossmann MG, Kuhn RJ. (2018) Flaviviruses have imperfect icosahedral symmetry. *Proc Natl Acad Sci USA* 115, 11608-11612.

St John SE, **Therkelsen MD**, Nyalapatla PR, Osswald HL, Ghosh AK, Mesecar AD. (2015) X-ray structure and inhibition of the feline infectious peritonitis virus 3C-like protease: Structural implications for drug design. *Bioorg Med Chem Lett* 25, 5072-5077.

Schmidt AG, **Therkelsen MD**, Stewart S, Kepler TB, Liao HX, Moody MA, Haynes BF, Harrison SC. (2015) Viral receptor-binding site antibodies with diverse germline origins. *Cell* 161, 1026-1034.

MacColl E, **Therkelsen MD**, Sherpa T, Ellerbrock H, Johnston LA, Jariwala RH, Chang W, Gurtowski J, Schatz MC, Mozammal Hossain M, Cassidy-Hanley DM, Clark TG, Chang WJ. (2015) Molecular genetic diversity and characterization of conjugation genes in the fish parasite *Ichthyopthirius multifiliis*. *Mol Phylogenet Evol* 86, 1-7.

Xu H, Schmidt AG, O'Donnell T, **Therkelsen MD**, Kepler TB, Moody MA, Haynes BF, Liao HX, Harrison SC, Shaw DE. (2015) Key mutations stabilize antigen-binding conformation during affinity maturation of a broadly neutralizing influenza antibody lineage. *Proteins* 83, 773-780.